All-propulsion design of the drag-free and attitude control of the European satellite GOCE

Acta Astronautica, 2009, 64, p. 325-344,

All-propulsion design of the Drag-Free and Attitude Control of the European Satellite GOCE

Enrico Canuto[a] , Luca Massotti[b,1]

[a]*Politecnico di Torino, Dipartimento di Automatica e Informatica, Corso Duca degli Abruzzi 24, 10129 Torino, Italy*

[b]*ESA Earth Observation Programme, Future Missions Division, ESTEC EOP-SF, Noordwijk NL-2200 AG*

Abstract

This paper concerns the drag-free and attitude control (DFAC) of the European Gravity field and steady-state Ocean Circulation Explorer satellite (GOCE), during the science phase. GOCE aims to determine the Earth's gravity field with high accuracy and spatial resolution, through complementary space techniques such as gravity gradiometry and precise orbit determination. Both techniques rely on accurate attitude and drag-free control, especially in the gradiometer measurement bandwidth (5mHz to 100mHz), where non-gravitational forces must be counteracted down to micronewton, and spacecraft attitude must track the local orbital reference frame with micro-radian accuracy. DFAC aims to enable the gravity gradiometer to operate so as to determine the Earth's gravity field especially in the so-called measurement bandwidth (5mHz to 100mHz), making use of ion and micro-thruster actuators. The DFAC unit has been designed entirely on a simplified discrete-time model (Embedded Model) derived from the fine dynamics of the spacecraft and its environment; the relevant control algorithms are implemented and tuned around the Embedded Model, which is the core of the control unit. The DFAC has been tested against uncertainties in spacecraft and environment and its code has been the preliminary model for final code development. The DFAC assumes an all-propulsion command authority, partly abandoned by the actual GOCE control system because of electric micro-propulsion not being fully developed. Since all-propulsion authority is expected to be imperative for future scientific and observation missions, design and simulated results are believed to be of interest to the space community.

[1] Corresponding author
E-mail addresses: Enrico.Canuto@polito.it (E. Canuto)
Luca.Massotti@esa.int (L. Massotti)

Acta Astronautica, 2009, 64, p. 325-344,

Keywords: Satellite attitude, drag free control, digital control.

1 Introduction: the GOCE mission

The scientific goal of the European space mission Gravity Field and Steady-state Ocean Circulation Explorer (GOCE) is to determine the stationary gravity field U, i.e. gravity anomalies $\Delta g(\theta,\lambda)$ down to 1 mGal (=10 μm/s^2), and geoid heights $N(\theta,\lambda)$ down to 1 cm, over the Earth's surface defined by latitude θ and longitude λ at a spatial resolution better than 100 km. The geoid is defined as the gravity equipotential surface approximating an ideal ocean surface at rest, known as the mean sea level (Figure 1). The geoid heights N refer to an Earth's reference ellipsoid and range from about –100 to 100 m. The geoid is the reference surface for all topography on land, ice and ocean.

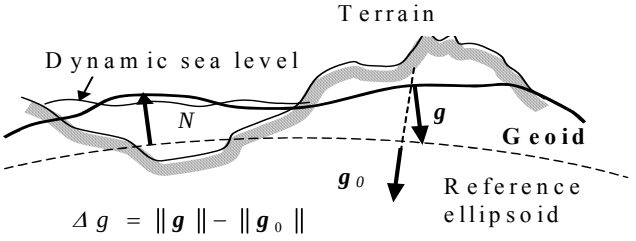

Figure 1. Earth's geoid and gravity anomaly

The gravity anomaly is the difference between the magnitude $g = \|\mathbf{g}(\theta,\lambda)\|$ of the actual gravity on the geoid and that of the normal gravity $g_0 = \|\mathbf{g}_0(\lambda)\|$ on a reference ellipsoid (Figure 1). Gravity anomalies are the surface mirror of the Earth's interior processes. Geoid heights and gravity anomalies [1], [16], are related to the Earth's gravitational potential U, which can be expanded into complex spherical harmonics $\bar{Y}_{nm}(\theta,\lambda)$ of degree n and order m, scaled by their complex spectrum $\bar{K}_{nm}$

$$U(r,\theta,\lambda) = \frac{\mu}{R}\sum_{n=0}^{\infty}\left(\frac{R}{r}\right)^{n+1}\sum_{m=-n}^{n}\bar{K}_{nm}\bar{Y}_{nm}(\theta,\lambda), \tag{1}$$

where R is the mean Earth radius, μ is the Earth gravitational constant, $r = R + h$, and h is the geodetic height.

According to [4], the traditional techniques of gravity field determination have reached their intrinsic limits. Any advances must rely on space techniques, because only they can provide global, regular and dense data sets of high and uniform quality. This concept has lead to space missions like the U.S. GRACE [2], the German CHAMP [3] and the European GOCE. The latter will implement three main concepts.

1) *Precise orbit determination* by satellite-to-satellite tracking. A low-Earth orbiter is equipped with a 12 channel receiver for the U.S. Global Positioning System (GPS). Taking their orbits and the GPS measurements of the low-Earth orbiter, the orbit of the spacecraft can be monitored to cm-precision without interruption. Satellite-to-satellite techniques are limited by the progressive attenuation of the gravitational field at satellite altitudes, which impedes the attainment of high spatial resolution. According to [4] at a low-Earth orbiter altitude $h = 250$ km the signal-to-noise ratio attains unity in the harmonic expansion of Eq. (1) around degree n=75, corresponding to a half-wavelength on the Earth's surface of about $\lambda_E / 2 = 250$ km.

2) *Satellite gravity gradiometry*. An on-board gradiometer measures the components of the gravity gradient tensor $\mathbf{U} = \nabla^2 U(r, \theta, \lambda)$ exploiting the classical differential approach to elucidate the effect of small-scale features. In this way, GOCE, the first gradiometry space mission, is expected to attain a unitary signal-to-noise ratio at a degree $n > 300$ in Eq. (1), i.e. at a half-wavelength $\lambda_E / 2 < 70$ km.

3) *Drag-free and attitude control* (DFAC). To extract gravity field components from orbit and gradiometer measurements, non-gravitational forces must be compensated by a drag-free control mechanism (see [5], [6], [7] [15], [18], [20], and [21]), and the spacecraft attitude must be accurately aligned to the local orbital reference frame (LORF), to which gravity measurements will be referred.

Satellite gradiometry and precise orbit determination by satellite-to-satellite tracking are complementary. By means of orbit determination it is possible to reconstruct the lower harmonics of the gravity field, while gradiometry provides better performance at medium and high harmonics. The intersection is somewhere close to $n = 15$ in Eq. (1), according to the analysis reported in [4]. This leads to the definition of a Measurement Bandwidth (MBW) for the gradiometer measurements,

$$\mathcal{F}_1 = \{ f_1 = 0.005 \le f \le f_2 = 0.1 \text{ Hz} \}, \tag{2}$$

i.e. the frequency region in which the measurement accuracy of the gravity gradient $\mathbf{U}$ has to be maximized. In fact, for a low-Earth orbiter like GOCE, having an orbital velocity $v_O \cong 7.8$ km/s, a measurement frequency of 0.1 Hz corresponds to an on-ground, spatial half-wavelength of about $\lambda_E / 2 = 78$ km, compatible with the resolution to be achieved, whereas 5 mHz corresponds to an on-ground separation of about 1560 km, which is the half-wavelength of the Earth potential harmonics of degree $n = 13$ in Eq. (1).

The GOCE satellite will fly on a circular (eccentricity $\varepsilon < 0.005$) sun-synchronous, dawn-dusk, quasi-polar orbit (inclination $i = 96.5°$) at a mean altitude $h \cong 250$ km, corresponding to the orbital rate

$$\omega_O = v_O / r = 2\pi f_O, \; r \cong 6630 \text{ km}, \; f_O \cong 0.19 \text{ Hz}. \tag{3}$$

The launch is planned to take place in autumn 2008 and the overall mission will last at least 20 months. To reduce the thermosphere[2] drag, the mission will take place during the early ascending leg of the solar activity cycle, whose minimum is foreseen to occur in the year 2007. The gradiometer measurements are planned to be collected in two or three phases of 6 months each.

2 The Gravity Gradiometer

The gravity gradiometer, developed by ONERA, France (see [23]), is an ensemble of three pairs of three-axial (3D) electrostatic accelerometers A_i (Figure 2). In each accelerometer a 0.32 kg proof mass is electro-statically suspended and actively positioned and aligned at the centre of a cage by means of voltages applied to electrodes machined on the internal walls of the cage. Capacitive sensors measure the proof mass displacement relative to the electrodes. The control voltages are proportional to the mass accelerations relative to the cage within the closed-loop control bandwidth $f_a \cong 20$ Hz . The 6 accelerometers are mounted two by two on three spacers, which keep the sensor centres apart at a fixed distance, the latter being known as the gradiometer baseline. An accelerometer pair A_iA_j, $ij = 14, 25, 36$, connected by its spacer, forms a one-axis gradiometer G_{ij} .

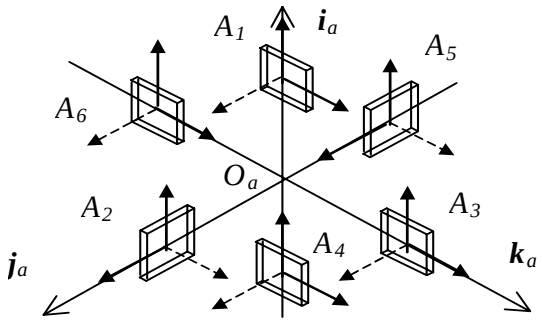

Figure 2. Layout of the gravity gradiometer.

On orbit, the cage-mass relative acceleration $\mathbf{a}_i$, $i = 1,...,6$, to be detected, can be written as

$$\mathbf{a}_i = -\mathbf{U}_O \mathbf{r}_i + \boldsymbol{\omega} \times \left(\boldsymbol{\omega} \times \mathbf{r}_i \right) + 2\boldsymbol{\omega} \times \dot{\mathbf{r}}_i + \dot{\boldsymbol{\omega}} \times \mathbf{r}_i + \mathbf{d} - \mathbf{p}_i \tag{4}$$

where $\mathbf{U}_O$ is the gravity-gradient tensor expressed in LORF coordinates, $\mathbf{r}_i$ is the position of the accelerometer centre with respect to the satellite centre-of-mass (CoM), the 2nd to 4th terms are the centrifugal, Coriolis and linear

[2] The neutral portion of the Earth's atmosphere between about 90 km to 600 km above the Earth surface is known as the thermosphere.

accelerations, respectively, caused by the satellite angular rate $\boldsymbol{\omega}$, $\mathbf{d}$ includes all non-gravitational accelerations acting on the spacecraft, and $\mathbf{p}_i$ accounts for self-gravity and electro-magnetic coupling. Extraction of the unknowns, namely $\mathbf{U}_O$, $\mathbf{d}$ and $\dot{\boldsymbol{\omega}}$, is accomplished by computing the common-mode and differential accelerations $\underline{\mathbf{a}}_{ij}$ and $\Delta\mathbf{a}_{ij}$, respectively, of each one-axis gradiometer G_{ij}

$$\underline{\mathbf{a}}_{ij} = \left(\mathbf{a}_i + \mathbf{a}_j\right)/2, \quad \Delta\mathbf{a}_{ij} = \left(\mathbf{a}_i - \mathbf{a}_j\right)/2 . \tag{5}$$

Each common-mode vector measures the non-gravitational component $\mathbf{a}_l = \mathbf{d}$ of the spacecraft CoM (linear) acceleration, whereas the differential terms measure the gravity gradient tensor $\mathbf{U}_O$ and the satellite angular acceleration $\mathbf{a}_a = \dot{\boldsymbol{\omega}}$. Ideally, separation of non-gravitational acceleration from gravity gradient tensor would imply no active drag compensation, except for maintaining altitude. Actually, misalignments and deviations from the nominal position generate accelerometer cross-couplings, whose effects on measurement accuracy can only be attenuated by on-orbit calibration and by active control of the spacecraft accelerations and attitude. Extensive studies have allocated the budget shown in Table 1 to gradiometer error sources [4]. The root mean square (RMS) of the gradiometer error components is expressed in milliEötvös ($1\ \text{mE} = 10^{-12}\ \text{s}^{-2}$).

Table 1 Gradiometer error allocation [mE]

Total	DFAC residuals	Spacecraft attitude	Instrument	Post-flight
4	1	2	3	1

3 DFAC technology and design steps

The paper illustrates the design methodology and the relevant simulated results of the attitude and drag free control unit, designed and tested during the design phase as a prototype for the final code development by the prime contractor. Drag-free and attitude control aims to enable the gradiometer to operate for the mission's scientific goals during the six-month operational phases. Planned or fault-driven transitions from/to other control operations are not treated here (see [8]). The DFAC technology is based on the following actuators and sensors.

1) A pair of ion thrusters, in cold redundancy, for along-track drag compensation (single-axis control).

2) Eight micro-thrusters, either electrical or cold-gas, for attitude tracking and compensation of lateral non-gravitational forces and torque disturbances (five-axis control). In the early design stages electrical propulsion was selected instead of cold-gas to meet the low noise constraint[3] (Section 4.3).
3) Gravity gradiometer for linear and angular acceleration measurement.
4) Two satellite-to-satellite (GPS) receivers, in cold redundancy, for the reference attitude determination from spacecraft CoM position and velocity.
5) Two star-tracker units, in cold redundancy, for attitude determination.

Sampling rate, range, digital resolution in number of bits and the time-step symbol of each control device are reported in Table 2. The following control issue follows from the same Table.

Control Issue 1. A multi-rate control has to be designed.

Table 2 DFAC actuators and sensors

Device	Sampling rate	Time subscript	Range	Number of bits
Ion thruster	$f_i = 10\text{Hz}$	i	1.5÷20mN	11
Micro thruster	$f_k = 2\text{Hz}$	k	0.002÷1.2mN (*)	10
Gradiometer	$f_i = 10\text{Hz}$	i	$\pm 20\mu\text{m/s}^2$	16
GPS receiver	$f_j = 1\text{Hz}$	j	Sufficient	32
Star tracker units	$f_k = 2\text{Hz}$	k	±1 (quaternion)	32
DFAC	$f_c = f_i$	i	NA	NA

(*) The range appears critical also for the forthcoming electrical micro-propulsion.

NA = not applicable

The DFAC was designed and implemented as an Embedded Model Control, a model/observer based design methodology inspired by [10] and treated in [11] (see also [22]). The design focal point is the construction of the discrete-time *embedded model* of the spacecraft to be controlled, and of the environment disturbance to be rejected. The model is embedded in the control unit, as the core of measurement and control algorithms.

Accordingly, the main design steps are the following.

1) Definition of drag-free and attitude control requirements in terms of some performance variables, derivation of sensor and actuator dynamics and noise, formulation of the class of the disturbance to be rejected (Section 4).

[3] Actually electrical micro-propulsion, being not mature, was abandoned forcing downsizing of drag-free requirements [19]. Micro-thrusting is kept in this paper being the key technology of future drag-free missions.

2) Construction of the Embedded (or design) Model made by the controllable and disturbance dynamics, to be observable from the measures. Formulation of the control problems in terms of performance variables and, only for attitude control, definition of the reference trajectories of the controllable state variables (Section 5).
3) Design of the attitude trajectory generator providing the local orbital reference frame (LORF); design of the state predictor and eigenvalue tuning to guarantee 'spacecraft' closed–loop stability against neglected dynamics. First eigenvalue tuning might take advantage of simple input-output operators of the modelling errors (Section 6).
4) Design of the DFAC algorithms in the form of state-feedback loops on the Embedded Model. Optimal drag-free and attitude command allocation to ion and micro-thruster assembly (Section 7).
5) Performance and robustness tests on the simulated spacecraft and environment (Section 8).

In the literature, drag-free and attitude control has been approached in the frequency domain, either employing H_∞ methodology (see [5] [12], [18], [20] and [21]) or simple PID strategies as in [13]. The frequency domain approach is attractive, because DFAC requirements are expressed in the same domain. The proposed formulation is mainly based on discrete-time state equations according to the cited methodology. Time-domain is essential for simulation and straightforward control algorithm design, implementation, set-up and testing. At first glance, it may appear to contrast with DFAC requirements as well as with disturbance classes, which are often formulated in the frequency domain through suitable PSD[4] (see Table 3 and Figure 5), but the latter can be profitably converted to time domain (see Section 5).

4 Control requirements and sensor/actuator dynamics and noise

This section illustrates the DFAC requirements which are referred to local orbital frame, as well as spacecraft dynamics and perturbations. Some details about sensor and actuator dynamics and noise are also provided. The resulting dynamic model to be simulated will be referred throughout as the 'fine model', as opposed to the design model.

4.1 Reference frames and control requirements

The inertial frame of the mission is the *J2000 Equatorial Reference Frame* $\mathcal{R}_J = \{O, \mathbf{i}_J, \mathbf{j}_J, \mathbf{k}_J\}$. The mission measurement frame is the *Local Orbital Reference Frame (LORF)* $\mathsf{R}_O = \{C, \mathbf{i}_O, \mathbf{j}_O, \mathbf{k}_O\}$. The origin C is the satellite CoM having inertial position $\mathbf{r}$ and velocity $\mathbf{v} = \dot{\mathbf{r}}$. The axes are defined by

[4] PSD means the square root of unilateral Power Spectral Densities throughout.

$$\mathbf{i}_O = \frac{\mathbf{v}}{\|\mathbf{v}\|},\ \mathbf{j}_O = \frac{\mathbf{r}\times\mathbf{v}}{\|\mathbf{r}\times\mathbf{v}\|},\ \mathbf{k}_O = \mathbf{i}_O \times \mathbf{j}_O . \tag{6}$$

In other words, $\mathbf{i}_O$ is aligned with the CoM velocity and points toward motion direction, $\mathbf{j}_O$ is aligned with the orbital angular momentum, $\mathbf{k}_O$ is slightly misaligned from $\mathbf{r}$ due to the low orbit eccentricity. The matrix $\mathbf{R}_O = |\mathbf{i}_O \quad \mathbf{j}_O \quad \mathbf{k}_O|$ is the LORF-to-inertial coordinates transformation, and defines the reference attitude to be tracked by the spacecraft during the mission. The orientation error $\mathbf{e}_O$, caused by the on-line estimate $\hat{\mathbf{R}}_O$, can be defined as

$$\begin{aligned} &\mathbf{R}_O\mathbf{E}_O = \hat{\mathbf{R}}_O,\ \mathbf{E}_O \cong I + \Delta\mathbf{E}_O \\ &\Delta\mathbf{E}_O = \begin{vmatrix} 0 & -e_{Oz} & e_{Oy} \\ e_{Oz} & 0 & -e_{Ox} \\ -e_{Oy} & e_{Ox} & 0 \end{vmatrix},\ \mathbf{e}_O = \begin{vmatrix} e_{Ox} \\ e_{Oy} \\ e_{Oz} \end{vmatrix}. \end{aligned} \tag{7}$$

Assuming circular orbit (eccentricity $\varepsilon < 0.005$), $\mathbf{e}_O$ can be shown to be related to position and velocity estimation errors $\Delta\mathbf{r}$ and $\Delta\mathbf{v}$ through

$$\mathbf{e}_O \cong \begin{vmatrix} -\Delta\mathbf{r}\cdot\mathbf{j}_O / r \\ \Delta\mathbf{r}\cdot\mathbf{i}_O / r - \Delta\mathbf{v}\cdot\mathbf{k}_O / v \\ \Delta\mathbf{v}\cdot\mathbf{j}_O / v \end{vmatrix},\ r = \|\mathbf{r}\|,\ v = \|\mathbf{v}\|. \tag{8}$$

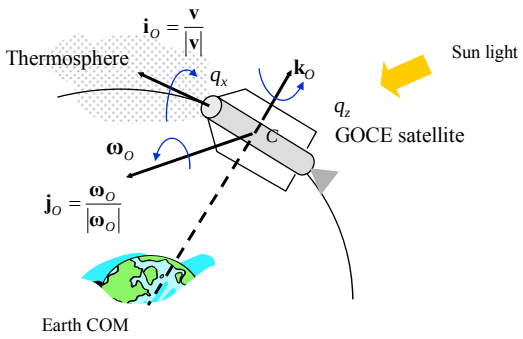

Figure 3. The Local Orbital Reference Frame.

The satellite body frame is the *Attitude Control Reference Frame* $\mathcal{R} = \{C, \mathbf{i}, \mathbf{j}, \mathbf{k}\}$, defined by spacecraft geometry and mass distribution. The spacecraft is a slender cylindrical body (about 5 m long) having octagonal cross-section with a diameter of about 1 m (Figure 4). The axis $\mathbf{i}$ coincides with the cylinder axis and points in the direction of motion. The solar panels are hinged on two opposite sides along lines parallel to $\mathbf{i}$, their mean plane defining $\mathbf{k}$. The axis $\mathbf{j}$

completes the frame and is positive opposite to the active side of the solar panels. The resulting frame is close to a principal axis frame, the products of inertia being less than 1%.

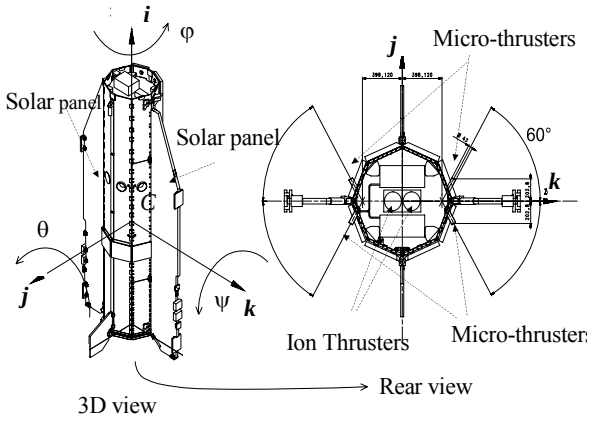

Figure 4. 3D view and enlarged rear section of the spacecraft.

The spacecraft attitude $\mathbf{q} = \{q_x, q_y, q_z\}$ is then defined by the body-to-LORF transformation

$$\mathbf{R}(\mathbf{q}) = \mathbf{Z}(q_z)\mathbf{Y}(q_y)\mathbf{X}(q_x) \tag{9}$$

where $\mathbf{X}(q_x)$, $\mathbf{Y}(q_y)$ and $\mathbf{Z}(q_z)$ are the usual roll, pitch and yaw rotations. The body frame is assumed to coincide with the gradiometer frame to which acceleration measurements are referred.

DFAC requirements, reported in Table 3 and derived from the gradiometer error allocation in Table 1, concern:

1) the residual non-gravitational CoM acceleration in body frame,
2) the spacecraft angular acceleration $\mathbf{a}_a = \dot{\boldsymbol{\omega}}$ and the angular rate $\Delta\boldsymbol{\omega} = \boldsymbol{\omega} - \mathbf{R}^T(\mathbf{q})\omega_O \mathbf{j}_O$, where ω_O is the angular rate of the osculating Keplerian orbit, and $\boldsymbol{\omega}$ and $\dot{\boldsymbol{\omega}}$ are in body coordinates,
3) the attitude $\mathbf{q}$ with respect to the LORF,
4) the LORF orientation error $\mathbf{e}_O$.

The symbols of the corresponding PSD are listed in Table 3: the underlined symbols, e.g. $\underline{S}_a$, denote the target bounds, which are shown in Figure 5 and are common to all components, whereas a second subscript, e.g. S_{ax}, selects a single component. The whole control frequency band, from zero frequency (DC) to $f_c / 2 = 5\text{Hz}$, has been partitioned into three regions:

1) the low-frequency band $\mathcal{F}_0 = \{f \le f_1\}$,
2) the MBW $\mathcal{F}_1$ and

3) the high-frequency band $\mathcal{F}_2 = \{ f_2 \le f \le f_c / 2 \}$.

Table 3 GOCE drag-free and attitude control requirements

Variable	PSD symbol	PSD (RMS) unit	$\mathcal{F}_0$	$\mathcal{F}_1$	$\mathcal{F}_2$
$\mathbf{a}_I$	$\underline{S}_I$	$\frac{\mu m}{s^2\sqrt{Hz}}$ $\left(\frac{\mu m}{s^2}\right)$	35 (0.5)	0.025	0.2
$\mathbf{a}_a = \dot{\boldsymbol{\omega}}$	$\underline{S}_a$	$\frac{\mu rad}{s^2\sqrt{Hz}}$ $\left(\frac{\mu rad}{s^2}\right)$	70 (1)	0.025	0.025
$\Delta\boldsymbol{\omega}$	$\underline{S}_\omega$	$\frac{\mu rad}{s\sqrt{Hz}}$ $\left(\frac{\mu rad}{s}\right)$	700 (10)	0.5	NA
$\mathbf{q}$	$\underline{S}_q$	$\frac{\mu rad}{\sqrt{Hz}}$ (μrad)	26000 (370)	7.9	NA
$\mathbf{e}_O$	$\underline{S}_O$	$\frac{\mu rad}{\sqrt{Hz}}$ (μrad)	14000 (200)	4.3	NA

As Table 3 and Figure 5 show, the most stringent requirements refer to MBW (solid lines in Figure 5), whereas relaxed requirements pertain to the low-frequency region, where the gravity field is estimated from precise orbit determination. The low-frequency bounds, originally expressed as RMS errors (values in brackets), have been converted to a constant PSD covering the region from DC to the 2nd orbital harmonics $2 f_O \cong 0.4\text{mHz}$, and are extrapolated toward the MBW by a decreasing line (about –40dB/decade steep). The resulting low-frequency bounds, shown as dashed lines in Figure 5, turn into requirements, which are more conservative yet reveal performance criticalities and margins as the result discussion will clarify (Section 8).

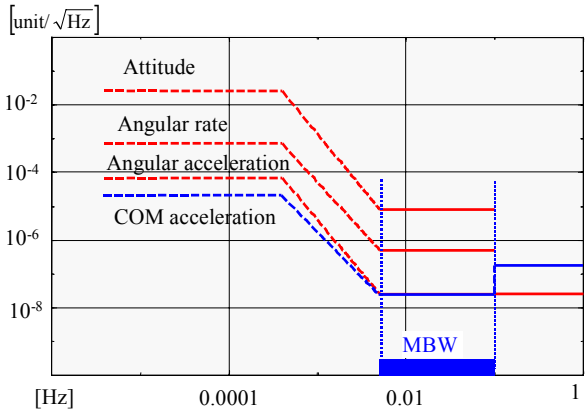

Figure 5. Piecewise PSD of the GOCE drag-free and attitude requirements.

The main control issue follows.

Control Issue 2. The DFAC must guarantee the target requirements as in Table 3 andFigure 5, under expected spacecraft and environment uncertainties.

4.2 Spacecraft dynamics and perturbations

4.2.1 Orbital and attitude state equations

The spacecraft motion is the combination of the inertial CoM orbital motion $\mathbf{r}$ and of the attitude $\mathbf{q}$ with respect to the LORF. The state equations of the spacecraft CoM motion are the following:

$$\begin{aligned}
&\dot{\mathbf{r}}(t) = \mathbf{v}(t), \quad \mathbf{r}(t_0) = \mathbf{r}_0 \\
&\dot{\mathbf{v}}(t) = -\mathbf{R}_E \mathbf{g}(t) + \mathbf{R}_O(\mathbf{r}, \mathbf{v}) \mathbf{R}(\mathbf{q}) \mathbf{a}_I(t), \ \mathbf{v}(t_0) = \mathbf{v}_0 \\
&\mathbf{a}_I(t) = \frac{1}{m}\left(\mathbf{F}_d(\mathbf{r}, \mathbf{v}, \mathbf{q}, t) + \mathbf{F}(t)\right)
\end{aligned} \tag{10}$$

In Eq. (10), $\mathbf{g} = \nabla U(\mathbf{r}_E)$ is the gravity acceleration converted into inertial coordinates by the Earth-fixed-to-inertial transformation R_E, $\mathbf{F}_d$ is the body vector of the environment forces (mainly thermosphere drag and wind), $\mathbf{F}$ is the body force actuated by the command thrusters, $\mathbf{a}_I$ is the residual non-gravitational acceleration in body coordinates to be zeroed by DFAC, $m \cong 1150\text{kg}$ is the spacecraft mass. Drag-free control is only concerned with the last equation, written in body frame. The whole CoM dynamics in (10) is the basis for the LORF real-time estimation from GPS measurements.

The attitude kinematics equation is obtained by expressing the angular rate $\Delta\boldsymbol{\omega}$ in body coordinates and is given by

$$\mathbf{Z}(q_z)\mathbf{Y}(q_y)\begin{vmatrix} \dot{q}_x \\ \dot{q}_y \\ 0 \end{vmatrix}(t) + \begin{vmatrix} 0 \\ 0 \\ \dot{q}_z \end{vmatrix}(t) = \mathbf{R}(\mathbf{q})\Delta\boldsymbol{\omega}(t), \ \mathbf{q}(0) = \mathbf{q}_0 \tag{11}$$

Under attitude control and neglecting coarse pointing not treated here, Eq. (11) can be simplified to be linear less higher order terms $\mathbf{o}_2(\cdot)$ which are significant to simulation but not to design, i.e.

$$\dot{\mathbf{q}}(t) = \Delta\boldsymbol{\omega}(t) + \mathbf{o}_2(\mathbf{q}, \Delta\boldsymbol{\omega}), \quad \mathbf{q}(0) = \mathbf{q}_0 . \tag{12}$$

Finally, the attitude dynamic equation is given by

$$\dot{\boldsymbol{\omega}}(t) = \mathbf{J}^{-1}\left(-\Delta\boldsymbol{\omega}(t) \times \mathbf{J}\Delta\boldsymbol{\omega}(t) + \mathbf{D}(t) + \mathbf{C}(t)\right), \ \Delta\boldsymbol{\omega}(0) = \Delta\boldsymbol{\omega}_0 \tag{13}$$

together with the following notations.

1) The inertia tensor $\mathbf{J}$ holds

$$\mathbf{J} = \begin{vmatrix} J_x = 153 & J_{xy} = -23 & J_{xz} = -6 \\ J_{xy} & J_y = 2691 & J_{yz} = 1 \\ J_{xz} & J_{yz} & J_z = 2653 \end{vmatrix} \text{kgm}^2 . \tag{14}$$

2) $\mathbf{C}$ is the body-coordinate command torque which is actuated by the micro-thrusters.

3) $\mathbf{D}$ is the total environment torque in body coordinates, defined by

$$\mathbf{D}(t) = \mathbf{C}_d(\mathbf{r}, \mathbf{v}, \mathbf{q}, t) + \mathbf{C}_g(t) + \mathbf{C}_m(t) . \tag{15}$$

4) $\mathbf{C}_d$ includes thermosphere drag and wind torques.

5) $\mathbf{C}_g$ is the gravity gradient torque, which depends on the gravity gradient tensor $\mathbf{U}_O$. Neglecting the products of inertia and linearizing around $\mathbf{q} = 0$ leads to the approximation

$$\mathbf{C}_g(t) \simeq \mathbf{R}^T(\mathbf{q})\mathbf{R}_O^T(\mathbf{r}, \mathbf{v}) 3\omega_O^2 \frac{\mathbf{r} \times J\mathbf{r}}{r^2} \simeq 3\omega_O^3 \begin{vmatrix} -(J_y - J_z) q_x(t) \\ (J_z - J_x) q_y(t) \\ 0 \end{vmatrix} . \tag{16}$$

6) $\mathbf{C}_m$, the magnetic torque, is the effect of the spacecraft magnetic dipole moment $\boldsymbol{\mu}$, mainly due to ion-thruster current, coupled with the Earth's magnetic field $\mathbf{b}_E$ as follows

$$\mathbf{C}_m(t) = \boldsymbol{\mu}(t) \times \mathbf{R}^T(\mathbf{q})\mathbf{R}_O^T(\mathbf{r}, \mathbf{v})\mathbf{R}_E \mathbf{b}_E(\mathbf{r}, t) . \tag{17}$$

Note the gravity gradient torque (16) makes pitch angle q_y locally unstable forcing the slender satellite to align with local Earth's gravity. Stability with respect to LORF is guaranteed by attitude control. To increase survivability, local stability is passively reinforced by tail fins, ensuring pitch to remain within fractions of a radian, which is sufficient for one-week survival (see [22]).

4.2.2 Environment forces and torques

Three environment fields have important effects on the GOCE satellite motion:

1) the Earth gravitational potential *U* and its anomalies (*n*>1 in Eq. (1)) determining the spacecraft orbit, under drag-free conditions, and the gravity gradient torque $\mathbf{C}_g$,

2) the thermosphere density and velocity field (wind) which couples with the orbital velocity $\mathbf{v}$ and the attitude $\mathbf{q}$ yielding the drag force $\mathbf{F}_d$ and torque $\mathbf{C}_d$,

3) the Earth magnetic field $\mathbf{b}_E$ which couples with the spacecraft magnetic dipole moment $\boldsymbol{\mu}$, yielding the magnetic torque $\mathbf{C}_m$.

Other perturbations like luni-solar gravitation and solar pressure have minor effects. It is outside the scope of this paper to deal with the fine models of gravity, drag and magnetic perturbations. A first issue is that these models should be accurate enough in a frequency region from DC to $f_c / 2 = 5\text{Hz}$, to test DFAC performances in a realistic manner. Therefore large-scale models have been integrated with small-scale ones, such as those accounting for small-scale thermosphere density variations [24]. A second concern stems from environment and spacecraft uncertainties. For instance, delayed launch, as will certainly occur, may severely affect drag magnitude, since this closely depends on solar activity. In addition, excessive drag magnitude might not be compatible with electrical propulsion. Uncertainty has been approached by defining nominal and worst-case perturbations and spacecraft. The performed analysis has shown that worst-case conditions do not affect accuracy performance but increase average and peak thrust, raising Control Issue 4 (see Section 4.3.1).

The time history (about half a day) of the nominal along-track force and the relevant PSD are shown in Figure 6. The latter rolls off at about –40dB/decade beyond the 2nd orbital harmonics $2 f_O \cong 0.4\text{mHz}$.

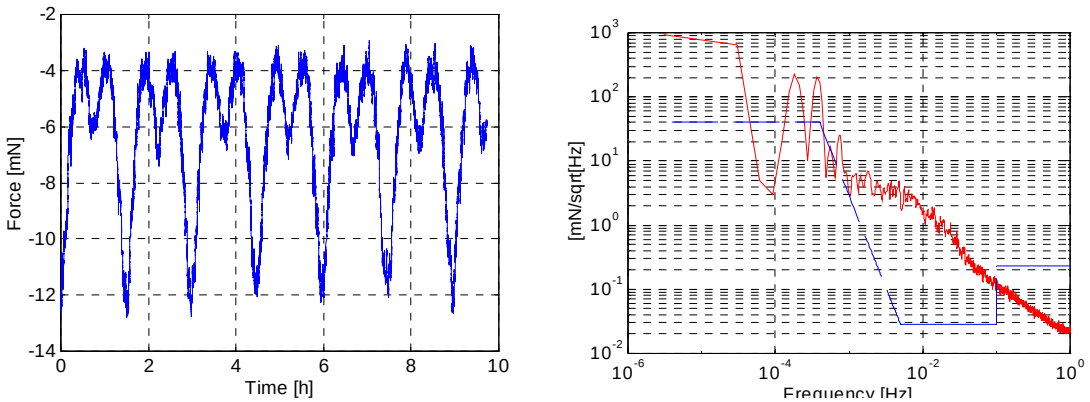

Figure 6. The along-track thermosphere drag. Left: time history (abscissa: hours, ordinates: mN). Right: PSD and the corresponding target bound (Ordinates: $\text{mN}/\sqrt{\text{Hz}}$)

Comparison with the residual acceleration bounds reported in Table 3 and in Figure 5, and repeated in Figure 6, raises the following Control Issue.

Control Issue 3. A DFAC bandwidth $f_x > f_2 = 0.1\text{Hz}$ (see Eq. (2)) is needed to compensate the along-track thermosphere drag F_{dx} below the target bound. A similar comparison suggests that DFAC bandwidths lower than f_x may be employed for compensating the lateral non-gravitational forces F_{dy} and F_{dz} as well as torque perturbations. The residual angular acceleration PSD S_a resulting from torque compensation must be compatible with attitude and angular rate requirements $\underline{S}_q$ and $\underline{S}_\omega$ (see Control Issue 7).

Table 4 summarizes the expected peak values of the force and torque components under worst-case (delayed launch) and nominal conditions (planned launch).

Table 4 Peak force [mN] and torque [nNm]

Case	F_{dx}	F_{dy}	F_{dz}	D_x	D_y	D_z
Worst	20.5	0.57	1.15	0.24	0.18	0.32
Nominal	12.8	0.36	0.72	0.07	0.14	0.1

4.3 Actuator and sensor dynamics and noise

4.3.1 Thruster dynamics and noise

Two types of thrusters are employed to actuate the DFAC (see Figure 7):

1) a pair of ion thrusters, *j=1,2,* in cold redundancy, to counteract the along-track drag F_{dx} in a wide frequency band from DC (altitude keeping) to MBW;
2) eight micro-thrusters, *j=1,…,8,* to counteract lateral non-gravitational forces F_{dy} and F_{dz} and to track the reference attitude defined by $\mathbf{R}_O$.

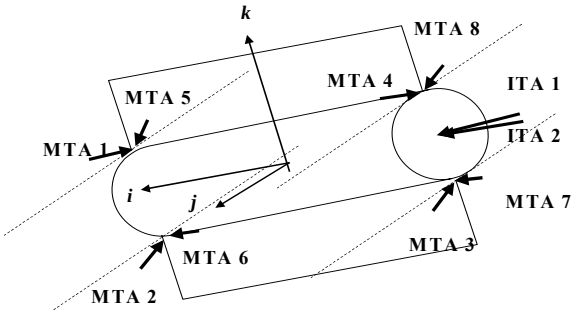

Figure 7. Layout of ion-thrusters (ITA 1 and 2) and micro-thrusters (MTA 1 to 8).

Let u_t denote the voltage command of the active ion-thruster and $\mathbf{u}_m$ the voltage command vector of the micro-thrusters. By neglecting their dynamic response, because of small settling times (<100 ms), a static voltage-to-force/torque relation may be written, depending on thruster geometry, scale factor and noise

$$\begin{vmatrix} F_x \\ F_y \\ F_z \\ \mathbf{C} \end{vmatrix} = \left[\begin{array}{c|c} B_{tx} & \Delta\mathbf{B}_{mx} \\ \hline \Delta B_{ty} & \mathbf{B}_{mz} \\ B_{tz} & \mathbf{B}_{my} \\ \Delta\mathbf{B}_{tq} & \mathbf{B}_{mq} \end{array}\right] \left(\begin{vmatrix} K_t & 0 \\ 0 & \mathbf{K}_m \end{vmatrix} \left(\left| \frac{u_t}{\mathbf{u}_m} \right| + \left| \frac{v_t}{\mathbf{v}_m} \right| \right) \right). \tag{18}$$

In Eq. (18) the force vector $\boldsymbol{F}$ has been decomposed into its components. The entries of the right-hand side first matrix depend on thruster geometry, while the prefix Δ indicates entries that should be zero from design. The second diagonal matrix contains the voltage-to-force scale factors. Finally v_t and $\mathbf{v}_m$ denote the thruster noise.

For use in drag-free missions [9], micro-thruster technology should ensure sub-micronewton noise in the MBW. The target parameters of the noise PSD are listed in Table 5 and the simulated PSD profiles are compared in Figure 8 with the linear acceleration bound of Table 3.

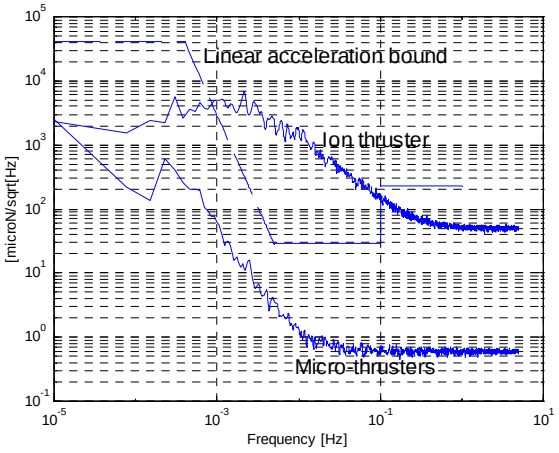

Figure 8. PSD of the thruster noise. Ordinate: $\mu\mathrm{N}/\sqrt{\mathrm{Hz}}$.

The number and layout of micro-thrusters (see Figure 7) enables average and peak thrust to be optimized. The former is proportional to power consumption, in case of electrical thrusters, or to propellant consumption, in case of cold gas. An excessive peak thrust might be very critical also for the forthcoming electrical micro-propulsion. Therefore a further Control Issue must be introduced.

Control Issue 4. The average thrust $\|\mathbf{u}_m\|_1$ and the largest peak $\|\mathbf{u}_m\|_\infty$, defined by

$$\begin{aligned} \|\mathbf{u}_m\|_\infty &= \max_{0\le t\le H,\,1\le j\le 8} \{u_{mj}(t)\} \\ \|\mathbf{u}_m\|_1 &= \frac{1}{H}\sum_{j=1}^{8}\int_0^H u_{mj}(\tau)\,d\tau \end{aligned} \tag{19}$$

have to be minimized, H being the longest duration of the gradiometer measurement phases.

Table 5 GOCE thruster noise requirements

Thruster	Low frequency		High frequency	
	Region [mHz]	Bound $\left[\mathrm{mN}/\sqrt{\mathrm{Hz}}\right]$	Region [mHz]	Bound $\left[\mathrm{mN}/\sqrt{\mathrm{Hz}}\right]$
Ion thruster	<2.8	5	>0.28	0.05
Micro-thruster	<0.34	0.5	>0.01	0.0006

4.3.2 Gradiometer dynamics and noise

As anticipated in Section 2, the accelerometer signal is the restoring voltage of a small proof-mass, driven by digital feedback [23]. A single-degree-of-freedom, simplified state equation of the overall closed-loop dynamics valid from MBW to gradiometer control rate (1 kHz) yields:

$$\begin{aligned} \begin{vmatrix} \dot{x} \\ \dot{v} \end{vmatrix}(t) &= \begin{vmatrix} 0 & 1 \\ -p^2 & -\alpha p \end{vmatrix} \begin{vmatrix} x \\ v \end{vmatrix}(t) + \begin{vmatrix} 0 & 0 \\ 1 & -1 \end{vmatrix} \begin{vmatrix} a + w_u \\ w_y \end{vmatrix}(t) \\ y(t) &= \begin{vmatrix} p^2 & \alpha p \end{vmatrix} \begin{vmatrix} x \\ v \end{vmatrix}(t) + w_y(t) \end{aligned}, \tag{20}$$

where x and v are the proof-mass position and velocity, a is the acceleration to be measured, y is the acceleration measure, w_u is the driving electronics noise and w_y is the sensor noise. The closed-loop bandwidth is given by $f_a = p/(2\pi) \cong 20\mathrm{Hz}$. By assuming noise components to have constant power spectral densities S_u^2 and S_y^2, the spectral density S^2 of the overall noise can be approximated as

$$S^2(f) = S_u^2 + \left(\frac{f}{f_a}\right)^4 S_y^2, \quad f_1 \le f \le f_a . \tag{21}$$

The PSD of the linear acceleration noise, given in Figure 9, agrees with the approximate expression in Eq. (21), showing an increasing slope at higher frequencies (f^2 noise). The same effect occurs in angular measurements, but it becomes significant at higher frequencies. Since gradiometer measures will be transmitted to DFAC at $f_c = 10\mathrm{Hz}$, the f^2 noise has to be appropriately filtered in order to avoid aliasing. A closer matching of gradiometer measurements to control strategies would have suggested including anti-aliasing in the DFAC chain, by feeding the latter with gradiometer raw measurements sampled at 1 kHz. On-board constraints prevented that solution, requiring anti-aliasing to be part of the gradiometer processing and raising the following issue.

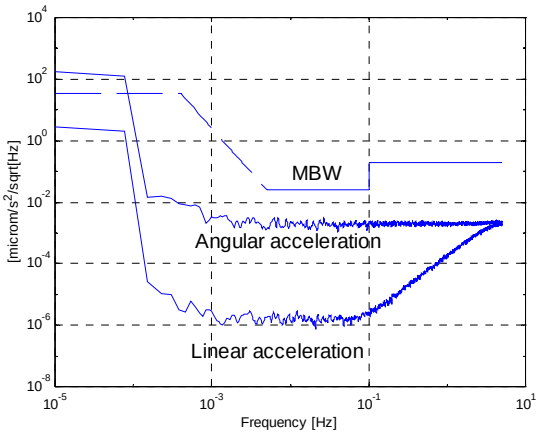

Figure 9. PSD of the gradiometer noise for common-mode (linear) and differential measures (angular).

Control Issue 5. DFAC strategies must be robust against delays and dynamics of the gradiometer and of the relevant data processing. They are aggravated by delays and dynamics of ion and micro-thrusters.

In addition, as Figure 9 shows, gradiometer measures are affected by random drift and bias. Then, the equation of the sampled, real-valued measure $\mathbf{y}_l$ of the linear acceleration $\mathbf{a}_l$ can be written as

$$\mathbf{y}_l(i) = \mathbf{a}_l(i) + \mathbf{v}_l(i) + \mathbf{b}_l(i) \tag{22}$$

where the measurement noise is written as the sum of $\mathbf{b}_l$ (drift and bias) and $\mathbf{v}_l$ (white and f^2 noise), and i is the gradiometer sampling time (see Table 2). A similar equation holds for the angular acceleration measure $\mathbf{y}_a$.

4.3.3 Attitude and position measurements

Tracking the local orbital frame (LORF) requires a pair of sensors:

1) CoM inertial *position and velocity* sensor: two GPS receivers, in cold redundancy, are employed. The vectors $\mathbf{y}_p$ and $\mathbf{y}_v$ denote the sampled, real-valued position and velocity measurements, corrupted by the measurement noise vectors $\mathbf{v}_r$ and $\mathbf{v}_v$, respectively, as follows

$$\mathbf{y}_r(j) = \mathbf{r}(j) + \mathbf{v}_r(j), \quad \mathbf{y}_v(j) = \mathbf{v}(j) + \mathbf{v}_v(j) \ , \tag{23}$$

j being the GPS sampling time (see Table 2).

2) Spacecraft inertial *attitude* sensor: a pair of star trackers, in cold redundancy, are employed. Let $\mathcal{R}_s = \{C, \mathbf{i}_s, \mathbf{j}_s, \mathbf{k}_s\}$ be the instrument frame of the active star tracker. The measurement provided by a star tracker is the instrument-to-inertial frame transformation $\mathbf{R}_S$, defined by

$$\mathbf{R}_s(k) = \mathbf{R}_O(k)\mathbf{R}(k)\mathbf{R}_{s0}\mathbf{V}_s(k) \tag{24}$$

where $\mathbf{R}_{s0}$ is the calibrated instrument-to-body transformation, $\mathbf{V}_s$ is the rotation defined by the instrument calibration errors and noise vector $\mathbf{v}_s$ (the so-called noise equivalent angle), $\mathbf{R}$ is the attitude matrix and *k* is the star-tracker sampling time (see Table 2). Using notations similar to Eq. (7), $\mathbf{V}_s$ can be approximated as $\mathbf{V}_s = I + \Delta\mathbf{V}_s$.

Timing and error properties of GPS and star tracker measures are summarized in Table 6 (see also Table 2).

GPS measurements are employed to on-line estimate the reference attitude frame $\mathbf{R}_O$. The contribution of the raw measurement noise $\mathbf{v}_r$ and $\mathbf{v}_v$ to the LORF orientation error $\mathbf{e}_O$, can be computed from Eq. (8), by imposing $\Delta\mathbf{r} = \mathbf{v}_r$, $\Delta\mathbf{v} = \mathbf{v}_v$ and assuming the noise components being white, Gaussian and statistically independent. Then, denoting the PSD of the *k*-th component of $\mathbf{e}_O$ with S_{Ok}, we have

$$\left|\begin{matrix} S_{Ox} \\ S_{Oy} \\ S_{Oz} \end{matrix}\right|(f) \cong \sqrt{2T_j}\left|\begin{matrix} \sigma_r / r \\ \sqrt{(\sigma_r / r)^2 + (\sigma_v / v)^2} \\ \sigma_v / v \end{matrix}\right| \le \left|\begin{matrix} 6.5 \\ 8.5 \\ 5.5 \end{matrix}\right| \frac{\mu\text{rad}}{\sqrt{\text{Hz}}}, \quad f \le \frac{1}{2T_j} = 0.5\text{Hz}, \tag{25}$$

having assumed rather conservative values as $\sigma_r = 30\text{m}$, $\sigma_v = 0.03\text{m/s}$ (see Table 6). Equation (25), showing values higher than Table 3, raises the following issue.

Control Issue 6. The design of the on-line LORF estimator must be such as to recover target accuracy in the MBW.

Table 6 GPS and star-tracker timing and errors.

Parameter	GPS		Star tracker 1 (2) [μrad]		
	Range	Rate	q_x	q_y	q_z
Noise (1σ)	30 m (σ_r)	0.03 m/s (σ_v)	20 (σ_{sx})	45 (100) (σ_{sy})	100 (45) (σ_{sz})
Bias	Negligible		±150 μrad		
Delay	Negligible		0.55 s		

Due to high noise - compare Table 6 to Table 3- star-tracker measurements must be averaged over time constants comparable to the MBW. In principle, this could prevent accurate attitude estimation, mainly because attitude will be affected by the integrated residual angular accelerations of the drag-free control. By allocating an equal attitude residual, say $\underline{S}_q / \sqrt{2}$, to both sources and by assuming the star-tracker measurements to be averaged by a 2nd order filter (see Section 7.2), worst case computation at $f = f_1 = 5\text{mHz}$ yields:

1) a new upper bound to residual angular acceleration (see Control Issue 3)

$$\frac{S_a}{(2\pi)^2 f_1^2} \le \frac{\underline{S}_q}{\sqrt{2}} \Rightarrow S_a \le 5\times 10^{-9} \frac{\text{rad}}{\text{s}^2\sqrt{\text{Hz}}} < \underline{S}_a \,, \tag{26}$$

2) an upper bound to the cut-off frequency f_q of the attitude filter

$$\sigma_s \sqrt{2T_k} \left(\frac{f_q}{f_1} \right)^2 \le \frac{S_q}{\sqrt{2}} \Rightarrow \; f_q \le (0.2 \div 0.5) f_1 \,, \tag{27}$$

the cut-off range depending on the attitude component. This raises the following issue.

Control Issue 7. The design of attitude estimator and feedback control must trade off between star tracker noise filtering and gradiometer drift compensation, in order to guarantee attitude and rate accuracies (see Table 3) in the frequency region from DC to the MBW.

5 The simplified design model

5.1 Main variables and DFAC requirements

The design model is a set of $n = 42$ discrete-time quasi-linear state equations forced by the thruster command vector $\mathbf{u}^T = \left| u_t \;\vdots\; \mathbf{u}_m^T \right|$ and a white noise vector $\mathbf{w}$, driving the dynamics of the unknown disturbance class $\mathcal{D}$ to be counteracted by the DFAC. The model *output* $\mathbf{y}_0$ is a vector of $n_y = 15$ state variables, namely the CoM position $\mathbf{y}_{0r} = \mathbf{r}$ and velocity $\mathbf{y}_{0v} = \mathbf{v}$, the spacecraft attitude $\mathbf{y}_{0q} = \mathbf{q}$ and the gradiometer linear and angular measures $\mathbf{y}_{0l}$ and $\mathbf{y}_{0a}$, free of low-frequency noise. The measurement vector $\mathbf{y}$ is defined at any discrete-time step *i* as the model output $\mathbf{y}_{0l}$ corrupted by the noise $\mathbf{v}$ and by the neglected dynamics operator $\partial\mathbf{P}$ as follows

$$\mathbf{y}(i) = \mathbf{y}_0(i) + \mathbf{v}(i) + \partial\mathbf{P}\left(\mathbf{y}_0\left(\mathbf{u}, \mathbf{w}\right)\right), \tag{28}$$

where $\partial\mathbf{P}$ is an input-output causal operator forced by the model output $\mathbf{y}_0$ [11]. It can be interpreted as a fractional error dynamics, expressing in time and frequency domain the dynamic percentage error (see the Appendix).

According to DFAC requirements in Table 3, the *performance variables* can be divided into:

1) residual linear and angular accelerations $\mathbf{a}_l$ and $\mathbf{a}_a$,

2) spacecraft attitude $\mathbf{q}$ and the residual attitude rate $\Delta\boldsymbol{\omega}^T = \left| \omega_x \quad \omega_O - \omega_y \quad \omega_z \right|$ with respect to orbital rate ω_O,

3) the orientation error $\mathbf{e}_O$ of the LORF R_O defining the reference attitude (see Section 4).

The DFAC must 'ideally' confine to zero the first two sets of variables and must estimate the LORF-to-inertial-frame transformation $\mathbf{R}_O$. The reference trajectories are

$$\underline{\mathbf{a}}_l = \underline{\mathbf{a}}_a = 0,\ \ \underline{\mathbf{q}} = 0,\ \ \underline{\omega}_x = \underline{\omega}_z = 0,\ \underline{\omega}_y = \omega_O\,. \tag{29}$$

5.2 Design model assumptions

The design model is derived from the fine model in Section 4 through a series of assumptions and a careful description of the unknown disturbance class $\mathcal{D}$ (see [14])Any disturbance class is modeled as a quasi-stationary random process forced by a white noise vector **w** through an asymptotically-stable state matrix $\mathbf{F}(\varepsilon)$ whose eigenvalues $\lambda(\mathbf{F})$ tend to the unit circle as far as $\varepsilon \to 0$. Since it is assumed that $\lim_{\varepsilon\to 0}\lambda(\mathbf{F}(\varepsilon)) = 1$, any disturbance component *d* might be described in the frequency domain by a PSD $S_d(f) = S_{d0}/f^m,\ 0<f<0.5/T$, *m* being the order of the sub-matrix of **F** relevant to *d* and S_{d0} the PSD at $f = 1Hz$. Here *m*=2 is assumed.

The resulting model is decomposed into two sub-models that are closely interconnected: the *orbital* dynamics and the *attitude* dynamics. For simplicity's sake, their state equations are in turn split into *thruster-to-gradiometer* equations $\mathbf{P}_l$ and $\mathbf{P}_a$ and *spacecraft* equations $\mathbf{P}_g$ and $\mathbf{P}_q$, where subscripts *a* and *q* refer to attitude, whereas *l* and *g* refer to orbit. Figure 10shows the model block diagram, free of the negelcted dynamics.

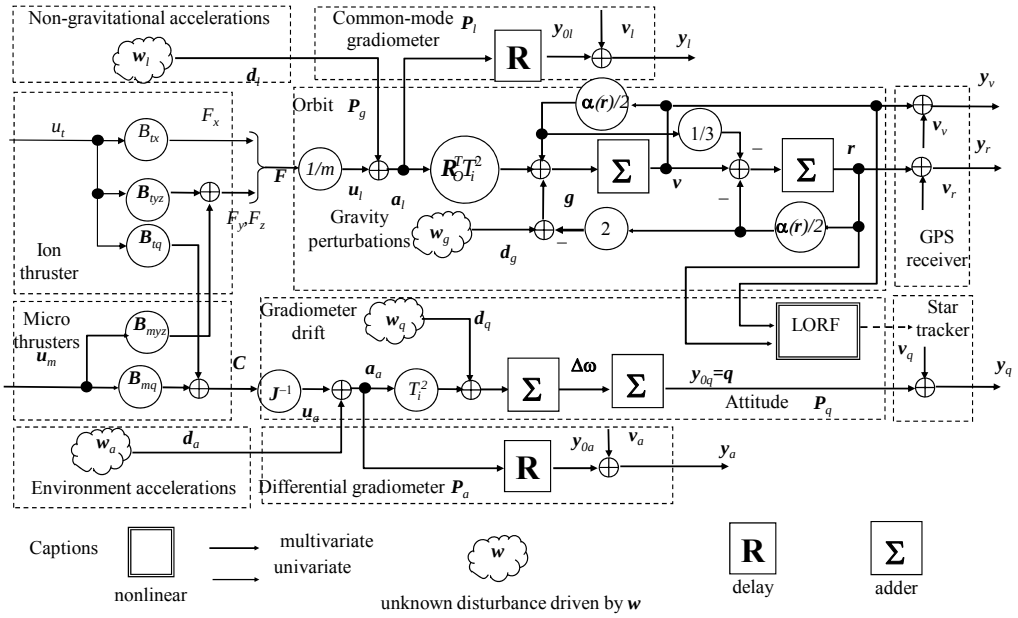

Figure 10. Block diagram of the Embedded (or design) Model.

The main assumptions relevant to both sub-models are the following,

1) *Single rate* (see Control Issue 1). The shortest time unit $T = T_i = 0.1$ s is adopted throughout, the generic discrete time being denoted by *i.* The measurements sampled at lower rates, namely $\mathbf{y}_r, \mathbf{y}_v$ and $\mathbf{y}_q$, are assumed to be sampled at T, but their valid samples are revealed at any time *i* by a vector $\tilde{\mathbf{u}}_y(i)$ of Boolean variables.

2) *Thruster-to-gradiometer dynamics* is approximated by a single-step delay, one for each linear and angular degree-of-freedom. It is the simplest (1st order) discrete-time dynamics, which is parameter-independent (robust) and dynamically conservative (long delay). In view of Control Issue 5, worst-case unmodelled dynamics have to be defined for the linear and angular measurement channels. They must account for all thruster and gradiometer gain and delay uncertainties.

3) *Gradiometer noise.* In the fine model (Section 4.3.2) the gradiometer noise of the angular channels is the sum of a high-frequency component $\mathbf{v}_a$ and of a low-frequency drift $\mathbf{b}_a$. The former is treated as the sole gradiometer noise, having a negligible impact on the DFAC performances (see Figure 9). The latter, on the contrary, if not adequately compensated by the DFAC, would drift the spacecraft attitude outside the prescribed tolerance. Since drift and bias are not observable from gradiometer measurements, but blend with the environment perturbations $\mathbf{d}_a$, the residual angular acceleration $\mathbf{a}_a$, at low frequencies, deviates from the real one acting on the spacecraft attitude. Such a deviations is corrected in the design model (see Figure 10) by adding an unknown disturbance $\mathbf{d}_q = -\mathbf{b}_a$ driven by $\mathbf{w}_q$ to the angular acceleration $\mathbf{a}_a$.

4) *Thruster noise.* The fine-model noise vectors v_t and $\mathbf{v}_m$, are treated as unknown perturbations to be compensated by the DFAC and therefore are included either in $\mathbf{d}_l$ or in $\mathbf{d}_a$. The same applies, because of their low magnitude, to the cross-coupling effects of micro-thrusters on the along-track command force F_x.

5) *Thruster cross-coupling effects.* The cross-coupling effects of the ion thruster on the lateral command forces F_y and F_z, and on the command torque $\mathbf{C}$, are on the contrary explicitly modelled. As a matter of fact, they dominate the amplitude of F_z, which would otherwise be negligible owing to low radial drag.

6) *Uniform scale.* All state variables of each sub-model are scaled to the same unit, namely: (i) length units [m] apply to $\mathbf{P}_g$, (ii) angular units [rad] to $\mathbf{P}_q$, (iii) linear acceleration units [m/s^2] to $\mathbf{P}_l$ and (iv) angular acceleration units [rad/s^2] to $\mathbf{P}_a$.

5.3 Orbital dynamics

State equations are split into two interconnected parts: (i) those modeling the thruster-to-gradiometer dynamics and (ii) those modelling the spacecraft CoM orbital motion in the inertial frame $\mathcal{R}_J$. Interconnection is assured by the residual acceleration $\mathbf{a}_l$. Orbital dynamics, although not controlled, determines the reference attitude.

5.3.1 Thruster-to-gradiometer state equation

Let $\mathbf{x}_l$ be the state vector, of size $n_l = 3\times(1+m_l) = 9$, of the thruster-to-gradiometer dynamics $\mathbf{P}_l$, but restricted to the linear channels. The state equation holds

$$\begin{aligned}
&\mathbf{x}_l(i+1) = \mathbf{A}_l\mathbf{x}_l(i) + \mathbf{G}_l\mathbf{w}_l(i) + \mathbf{B}_l\mathbf{u}(i), \quad \mathbf{x}_l(0) = \mathbf{x}_{l0} \\
&\mathbf{y}_l(i) = \mathbf{C}_l\mathbf{x}_l(i) + \mathbf{v}_l(i) + \partial\mathbf{P}_l\left(\mathbf{y}_{l0}\left(\mathbf{u},\mathbf{w}_l\right)\right) \\
&\mathbf{y}_{l0}(i) = \mathbf{C}_l\mathbf{x}_l(i)
\end{aligned}, \tag{30}$$

$\partial\mathbf{P}_l$ is the modeling error, and the following notations, with the help of (18), apply

$$\begin{aligned}
&\mathbf{x}_l = \begin{vmatrix}\mathbf{y}_{l0}\\ \mathbf{z}_l\end{vmatrix}, \mathbf{A}_l = \begin{vmatrix}0 & \mathbf{H}_l\\ 0 & \mathbf{F}_l\end{vmatrix}, \mathbf{G}_l = I, \mathbf{C}_l = \begin{vmatrix}I & 0\end{vmatrix} \\
&\mathbf{B}_l = \begin{vmatrix}\mathbf{B}_{tl}/m & \vdots & \mathbf{B}_{ml}/m\\ & 0 & \end{vmatrix}, \mathbf{B}_{tl} = \begin{vmatrix}B_{tx}\\ \Delta B_{ty}\\ B_{tz}\end{vmatrix}, \mathbf{B}_{ml} = \begin{vmatrix}0\\ \mathbf{B}_{my}\\ \mathbf{B}_{mz}\end{vmatrix}
\end{aligned}. \tag{31}$$

The 1st diagonal block of $\mathbf{A}_l$ is identically zero according to Assumption 2: a single-step delay models the thruster-to-gradiometer dynamics. The vector $\mathbf{z}_l$ is the state modelling the unstable dynamics of the class of the unknown non-gravitational accelerations $\mathbf{d}_l = \mathbf{H}_l\mathbf{z}_l + \mathbf{G}_{l0}\mathbf{w}_l$. The size $3\times m_l = 6$ of $\mathbf{z}_l$ has been designed to match the drag PSD (see Figure 8) especially in the MBW. The pair $(\mathbf{C}_l, \mathbf{A}_l)$ is observable, while the pair $(\mathbf{A}_l, \mathbf{B}_l)$ is neither controllable nor stabilizable, due to the unitary eigenvalues of $\mathbf{F}_l$ in Eq. (31). The residual linear acceleration $\mathbf{a}_l$ is given by

$$\mathbf{a}_l(i) = \left(\mathbf{B}_{tl}u_t(i) + \mathbf{B}_{ml}\mathbf{u}_m(i)\right)/m + \mathbf{d}_l(i). \tag{32}$$

By neglecting thruster and gradiometer cross-couplings as well as weak non-linear effects, a generic diagonal element of the error dynamics $\partial\mathbf{P}_l$, written in fractional form, can be approximated by (see the Appendix)

$$\partial\mathbf{P}_l(f) = \frac{y_l(f) - y_{l0}(f) - v_l(f)}{y_{l0}(f)} \cong 0.5\frac{\left(e^{j2\pi f} - 0.55\right)^2}{\left(e^{j2\pi f} + 0.05\right)^2}, \quad |f| \le 0.5/T = f_{\max} = 5\text{Hz}. \tag{33}$$

The coefficients in (33) depend on the thruster and gradiometer scale factor errors, less than 10%, and on the gradiometer anti-aliasing dynamics. The harmonic magnitude is monotonically increasing (see Figure 14) and satisfies

$$\lim_{f\to 0}\left|\partial\mathbf{P}_l(f)\right| << 1, \quad \max_{|f|\le 0.5/T}\left|\partial\mathbf{P}_l(f)\right| < 2\,. \tag{34}$$

Lower and higher frequency inequalities in Eq. (34) imply model error to increase in percentage from low to higher frequency as expected and to overcome the 100% threshold as the DFAC Nyquist frequency $f_{\max} = 0.5/T$ is approached.

5.3.2 Orbital state equations

The main modeling issue, driven by Control Issue 7, concerns how to model the gravity acceleration $\mathbf{g}$, avoiding the spherical harmonics expansion of Eq. (1), and favoring the reference trajectory generator (see Section 3) to recover the target accuracy of the orientation error $\mathbf{e}_O$ in the MBW (Control Issue 7). This is obtained by expressing $\mathbf{g}$ as the sum of a *known function* $\mathbf{g}_0(\mathbf{r})$ of the orbital state variables, and of an *unknown disturbance* $\mathbf{d}_g$ driven by $\mathbf{w}$. The accuracy of the latter component is affected by the LORF generator bandwidth, which has to be designed quite narrow, in order to filter out the noise of the GPS position and velocity measurements. The former component is only sensitive to the initial errors of the orbital state variables, which are completely recovered within the generator settling time. Therefore the gravity model is written as

$$\begin{aligned}
&\mathbf{g} = \mathbf{g}_0(\mathbf{r}) + \mathbf{d}_g,\ \mathbf{g}_0(\mathbf{r}) = -\boldsymbol{\gamma}_0(\mathbf{r})\mathbf{r} \\
&\boldsymbol{\gamma}_0(\mathbf{r}) = \underline{\omega}_O^2\left(I + \begin{vmatrix} \delta\alpha_x(r,r_z) & 0 & 0 \\ 0 & \delta\alpha_y(r,r_z) & 0 \\ 0 & 0 & \delta\alpha_z(r,r_z) \end{vmatrix}\right),\ \left|\delta\alpha_{x,y,z}\right| \le 0.01
\end{aligned}, \tag{35}$$

where $\underline{\omega}_O$ is the average orbital angular rate and the terms like $\delta\alpha_x$ are corrections accounting for the variable satellite radius *r* and the J_2 term of the spherical harmonics expansion (Earth's polar flattening).

Let $\mathbf{x}_g$ denote the overall state vector of the orbital dynamics $\mathbf{P}_g$, having size $n_g = 3\times(2+m_g) = 12$. Then the orbital state equation, which is driven by the white noise $\mathbf{w}_g$ and by the residual non-gravitational accelerations $\mathbf{a}_l$, is written as

$$\begin{aligned}
&\mathbf{x}_g(i+1) = \mathbf{A}_g(\mathbf{r})\mathbf{x}_g(i) + \mathbf{G}_g\mathbf{w}_g(i) + \mathbf{B}_g(\mathbf{r},\mathbf{v})\mathbf{a}_l(i),\ \mathbf{x}_g(0) = \mathbf{x}_{g0} \\
&\begin{vmatrix}\mathbf{y}_r \\ \mathbf{y}_v\end{vmatrix}(i) = \begin{vmatrix}\mathbf{C}_r \\ \mathbf{C}_v\end{vmatrix}\mathbf{x}_g(i) + \begin{vmatrix}\mathbf{v}_r \\ \mathbf{v}_v\end{vmatrix}(i),
\end{aligned}, \tag{36}$$

with the following notations

$$\mathbf{x}_g = \begin{vmatrix} \mathbf{r} \\ \mathbf{v} \\ z_g \end{vmatrix}, \quad \mathbf{A}_g = \begin{vmatrix} I - \boldsymbol{\alpha}/2 & I - \boldsymbol{\alpha}/6 & 0 \\ -\boldsymbol{\alpha} & I - \boldsymbol{\alpha}/2 & \mathbf{H}_g \\ 0 & 0 & \mathbf{F}_g \end{vmatrix}, \ \mathbf{G}_g = \begin{vmatrix} 0 \\ \mathbf{G}_{gv} \\ \mathbf{G}_{gz} \end{vmatrix}, \ \mathbf{B}_g = \begin{vmatrix} 0 \\ T_i^2 \mathbf{R}_O^T \\ 0 \end{vmatrix}, \quad \begin{vmatrix} \mathbf{C}_r \\ \mathbf{C}_v \end{vmatrix} = \begin{vmatrix} I & 0 & 0 \\ 0 & I & 0 \end{vmatrix}, \ \boldsymbol{\alpha} = \gamma_0(\mathbf{r}) T_i^2 \ . \quad (37)$$

The vector $\mathbf{z}_g$ is the state vector modeling the unstable dynamics of the unknown gravitational perturbations $\mathbf{d}_g = \mathbf{H}_g \mathbf{z}_g + \mathbf{G}_{zv} \mathbf{w}_g$. The size $3 \times m_g = 6$ of $\mathbf{z}_g$ has been designed to match the PSD of the gravitational anomalies in the MBW. The pair $\left(\left| \mathbf{C}_r \quad \mathbf{C}_v \right|^T, \mathbf{A}_g \right)$ is observable and the pair $\left(\mathbf{A}_g, \mathbf{B}_g \right)$ is neither controllable nor observable because of the unitary eigenvalues of the disturbance state matrix $\mathbf{F}_g$. Eq. (36) is affected by structured uncertainty because of the erroneous $\boldsymbol{\alpha}$ in (37); robust stability conditions are treated in [17]

5.4 Attitude dynamics

5.4.1 Thruster-to-gradiometer dynamics

Let $\mathbf{x}_a$ be the state vector, of dimension $n_a = 3 \times (1 + m_a) = 9$, of the thruster-to-gradiometer dynamics $\mathbf{P}_a$, restricted to angular accelerations. The relevant state equation and design considerations are the same as in Section 5.3.1, upon replacement of subscript *l* with *a*.

5.4.2 Attitude dynamics

The main assumptions are the following:

1) Dynamic imbalance due to a non-spherical inertia tensor $\mathbf{J}$ as in Eq. (14) and gravity gradient torque are not explicitly modeled, but included in $\mathbf{d}_a$. This is justified first by their low-frequency resonance, being of the same order of the orbital frequency $f_O \cong 0.2$ mHz, and second by the bound to angular rates $|\omega_x|, |\omega_z| \le 30$ μrad/s (see Table 3). Treating them as an unknown disturbance, corresponds to affecting the design model with structured uncertainties, thus requesting stability proof. The latter is guaranteed by providing the attitude state predictor with a sufficient BW not lower than f_O. Details are omitted (see [22]

2) The attitude measurement white noise $\mathbf{v}_q$ accounts for a pair of error sources: the random components $\mathbf{v}_S$ of the star-tracker errors (the so-called noise equivalent angle) and the LORF orientation error $\mathbf{e}_O$. Using matrix notations introduced in Section 4, the attitude error matrix $\mathbf{V}_q$ can be shown to satisfy

$$\mathbf{V}_q \cong I + \Delta\mathbf{V}_q, \quad \Delta\mathbf{V}_q \cong \mathbf{R}_{s0} \Delta\mathbf{V}_s \mathbf{R}_{s0}^T - \Delta\mathbf{E}_O \ , \quad (38)$$

implying the attitude noise statistics depends on the active unit.

Let $\mathbf{x}_q$ denote the overall state vector of the attitude dynamics $\mathbf{P}_q$, having size $n_q = 3\times\left(2+m_q\right)$. Then the state equation driven by the residual angular accelerations $\mathbf{a}_a$ and the white noise $\mathbf{w}_q$, is:

$$\begin{aligned}&\mathbf{x}_q(i+1) = \mathbf{A}_q\mathbf{x}_q(i) + \mathbf{G}_q\mathbf{w}_q(i) + \mathbf{B}_q\left(\mathbf{q}\right)\mathbf{a}_a(i),\ \mathbf{x}_q(0) = \mathbf{x}_{q0}\\ &\mathbf{y}_q(i) = \mathbf{C}_q\mathbf{x}_q(i) + \mathbf{v}_q(i)\end{aligned}, \tag{39}$$

with the following notations

$$\mathbf{x}_q = \begin{vmatrix}\mathbf{q}\\ \Delta\boldsymbol{\omega}\\ z_q\end{vmatrix}, \mathbf{A}_q = \begin{vmatrix}I & I & 0\\ 0 & I & \mathbf{H}_q\\ 0 & 0 & \mathbf{F}_q\end{vmatrix}, \mathbf{G}_q = \begin{vmatrix}0\\ \mathbf{G}_{q\omega}\\ \mathbf{G}_{qz}\end{vmatrix},\ \mathbf{B}_q = \begin{vmatrix}0\\ T_i^2\mathbf{J}^{-1}\\ 0\end{vmatrix}; \mathbf{C}_q = \begin{vmatrix}I\\ 0\\ 0\end{vmatrix}^T. \tag{40}$$

6 Attitude and drag-free control

6.1 Architecture

Digital control design becomes a rather straightforward task, provided that the design model is available. A standard architecture, respecting the conceptual steps mentioned in Section 3, is pursued, including a *reference trajectory generator* providing the state variables to be tracked (the LORF), *state predictors* driven by measurements and commands, to provide the one-step prediction of the controllable states and of the unknown disturbances to be rejected, *control laws* creating the commands as a combination of the trajectory errors and of the known and predicted disturbance terms. When, as in this case, more actuators than necessary are available, the control law is also in charge of distributing the command components to them, according to some optimality criterion. We prefer to speak of state prediction rather than state observer, as the one-step prediction of the state must feed the control law to naturally recover the computation delay.

Here, for simplicity, sensors and actuators are assumed to be sampled at the highest rate *1/T*=10 Hz. The micro-thruster command $\mathbf{u}_m$ is computed at the highest rate and then dispatched to micro-thrusters at their own rate. GPS and star-tracker measurements, actually sampled at a lower rate, are treated according to a predictor-corrector scheme. The predictor works at the highest rate, the corrector at the measurement rate (see Control Issue 1).

Table 7 Threshold frequencies for attitude control.

Variable	Frequency	Value	Unit
Angular rate	f_ω	8	mHz

Attitude	f_q	9	mHz
MBW lower limit	f_1	5	mHz

Two decomposition patterns are adopted to deal with model complexity.

Hierarchical decomposition. The drag-free control, according to Control Issue 3, should be a wide-band inner feedback loop (gradiometer-to-thruster), which may be designed separately from attitude control. Attitude (and rate) control should rather be a narrow-band outer feedback loop (star-tracker to thrusters) to compensate slowly varying drifts (like gradiometer drift) below certain threshold frequencies, dictated among others by the star-tracker noise. With regard to attitude, such frequencies can be roughly estimated by equating attitude (and rate) target bounds to the PSD computed by integrating the acceleration bound in the MBW. Table 7 shows that such frequencies approach the lower extreme of the MBW, helping to solve Control Issue 6.

Coordinate decomposition. Inner and outer feedback loops can be decomposed into three parallel loops, one for each spacecraft CoM and attitude coordinate. Cross-couplings are treated as known internal disturbances.

The control block-diagram is shown in Figure 11. Distinction is made between real-valued commands and measures $\mathbf{u}, \mathbf{y}$, internal to control algorithms, and their digital values $\tilde{\mathbf{u}}$, to be dispatched to thruster drivers, and $\hat{\mathbf{y}}$, received from sensors electronics.

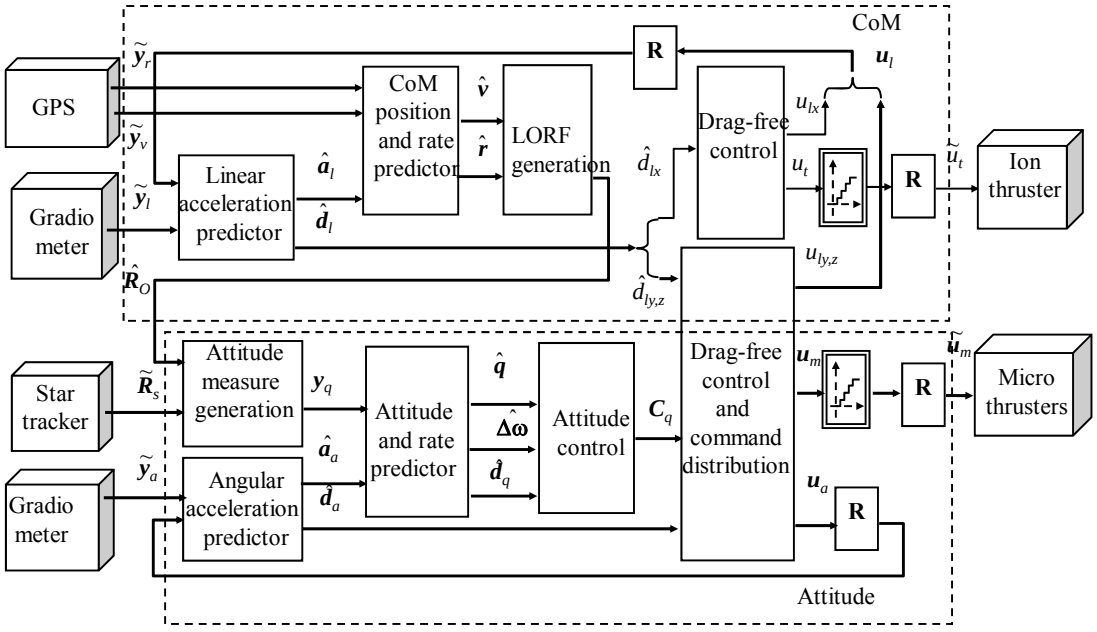

Figure 11. Block diagram of the attitude and drag-free control.

6.2 Reference trajectory generator

The reference trajectory generator is a state predictor estimating the inertial spacecraft CoM position $\hat{\mathbf{r}}$ and velocity $\hat{\mathbf{v}}$. Thus, the LORF transformation $\hat{\mathbf{R}}_O$ is one-step predicted. The state predictor is a constrained-gain one [11], taking advantage of the coordinate decomposition and of the error-free kinematics. The key manoeuvre, to improve measurement noise filtering (Control Issue 7) is to constrain the correction vector to the form:

$$\mathbf{G}_g \left| \mathbf{L}_r \,\vdots\, \mathbf{L}_v \right| \begin{vmatrix} \mathbf{y}_r(i) - \mathbf{C}_r \hat{\mathbf{x}}_g(i) \\ \mathbf{y}_v(i) - \mathbf{C}_v \hat{\mathbf{x}}_g(i) \end{vmatrix}, \tag{41}$$

in other words to belong to the range of $\mathbf{G}_q$, which is lower than the state space size. In this case, unlike in the attitude state-predictor in Section 7.2, constraining the predictor gain does not jeopardize stability, because of the multivariate measures (position and velocity). The predictor state equation is thus

$$\begin{aligned} &\hat{\mathbf{x}}_g(i+1) = \mathbf{A}_g\left(\hat{\mathbf{r}}\right)\hat{\mathbf{x}}_g(i) + \mathbf{B}_g\left(\hat{\mathbf{r}},\hat{\mathbf{v}}\right)\hat{\mathbf{a}}_l(i) + \mathbf{G}_g\left|\mathbf{L}_r\left(\hat{\mathbf{r}}\right) \,\vdots\, \mathbf{L}_v\left(\hat{\mathbf{r}}\right)\right| \begin{vmatrix} \mathbf{y}_r(i) - \mathbf{C}_r \hat{\mathbf{x}}_g(i) \\ \mathbf{y}_v(i) - \mathbf{C}_v \hat{\mathbf{x}}_g(i) \end{vmatrix} \\ &\begin{vmatrix} \hat{\mathbf{y}}_r \\ \hat{\mathbf{y}}_v \end{vmatrix}(i) = \begin{vmatrix} \mathbf{C}_r \\ \mathbf{C}_v \end{vmatrix} \hat{\mathbf{x}}_g(i), \quad \begin{vmatrix} \mathbf{y}_r \\ \mathbf{y}_v \end{vmatrix}(i) = \begin{vmatrix} \rho_r \tilde{\mathbf{y}}_r \\ \rho_v \tilde{\mathbf{y}}_v \end{vmatrix}(i), \hat{\mathbf{x}}_g(0) = \hat{\mathbf{x}}_{g0} \end{aligned}, \tag{42}$$

where ρ_r, ρ_v are the quantization levels. Observer gain matrices $\mathbf{L}_r\left(\hat{\mathbf{r}}\right), \mathbf{L}_v\left(\hat{\mathbf{r}}\right)$ are shown to be dependent on the position estimate $\hat{\mathbf{r}}$. This is necessary to keep constant the state-predictor eigenvalues, collected in the set Λ_g. The LORF matrix $\hat{\mathbf{R}}_O$ and the orbital rate $\hat{\omega}_O$ are then computed using equations (7) and (43) respectively. More details can be found in [17].

6.3 Drag-free control law and command distribution

The drag-free control follows by forcing $\mathbf{a}_l(i) = 0$ in Eq. (32) as well as putting $\mathbf{a}_a(i) = 0$. Then, by introducing the one-step predictions $\hat{\mathbf{d}}_l(i)$ and $\hat{\mathbf{d}}_a(i)$ of the unknown disturbances and the attitude control torque $\mathbf{C}_q$, the control equation results:

$$\begin{aligned} &u_t(i) = -m\hat{d}_{lx}(i)/B_{tx},\ \tilde{u}_t(i) = \mathrm{int}\left(u_t(i)/\rho_t\right),\ \tilde{u}_{t,\min} \le \tilde{u}_t(i) \le \tilde{u}_{t,\max} \\ &\mathbf{B}_m \mathbf{u}_m(i) = \begin{vmatrix} \mathbf{B}_{my} \\ \mathbf{B}_{mz} \\ \mathbf{B}_{mq} \end{vmatrix} \mathbf{u}_m(i) = -\begin{vmatrix} B_{ty} \\ B_{tz} \\ \mathbf{B}_{tq} \end{vmatrix} u_t(i) - \begin{vmatrix} m\hat{d}_{ly} \\ m\hat{d}_{lz} \\ \mathbf{J}\hat{\mathbf{d}}_a \end{vmatrix}(i) + \begin{vmatrix} 0 \\ 0 \\ \mathbf{C}_q \end{vmatrix}(i) \\ &\tilde{\mathbf{u}}_m(i) = \mathrm{int}\left(\mathbf{u}_m(i)/\rho_m\right),\ 0 \le \tilde{\mathbf{u}}_m(i) \le \tilde{\mathbf{u}}_{m,\max} \end{aligned}, \tag{43}$$

where $\mathrm{int}(\cdot)$ signifies rounding off, and ρ_t and ρ_m are the command quantization levels.

The first equation can be directly solved in the command voltage $u_t(i)$ to be dispatched to ion-thruster after digitization. The second equation is a set of five linear equations in $n_m = 8$ unknowns, namely the voltage commands to micro-thrusters collected in the vector $\mathbf{u}_m(i)$. Control Issue 4 requires this equation to be solved by minimizing average and maximum thrust, which implies solving a linear programming (LP) problem at each step [22]. An efficient, fixed-time solution minimizing the average thrust has been found by exploiting the lower dimensionality of the dual simplex and some peculiarities of $\mathbf{B}_m$ (LP strategy). Peak reduction is instead favored by the relaxed requirements on the cross-axis residual linear accelerations (a_{ly}, a_{lz}) below the MBW and by the negligible effect on the orbit drift of the corresponding non-gravitational perturbations d_{ly}, d_{lz}. To this end, the average and the orbital harmonics of d_{ly}, d_{lz} are filtered out from their estimates $\hat{d}_{ly}, \hat{d}_{lz}$ and therefore are not rejected (LF strategy)

6.4 Attitude control law

Attitude control must first stabilize Eq. (39) around the attitude and rate reference trajectories defined in Eq. (29). Then, it must force to zero the residual acceleration $\mathbf{a}_a + \mathbf{d}_q$, affected by the low-frequency drift and bias of the gradiometer noise. The feedback control law results

$$\mathbf{C}_q(i) = \mathbf{J}\left(-\mathbf{K}_1\hat{\mathbf{q}}(i) + \mathbf{K}_2\Delta\hat{\boldsymbol{\omega}}(i) - \hat{\mathbf{d}}_q(i)\right)/T_i^2, \tag{44}$$

where, exploiting coordinate decomposition, the feedback gain matrices $\mathbf{K}_1$ and $\mathbf{K}_2$ become diagonal and their values depend on the closed-loop attitude eigenvalue set Λ_{cq}.

7 State predictors and eigenvalue tuning

7.1 Acceleration state-predictor

Referring to linear accelerations, the state-predictor follows directly from Eq. (30) and the following holds

$$\begin{aligned} &\hat{\mathbf{x}}_l(i+1) = \mathbf{A}_l\hat{\mathbf{x}}_l(i) + \mathbf{L}_l\left(\mathbf{y}_l(i) - \mathbf{C}_l\hat{\mathbf{x}}_l(i)\right) + \mathbf{B}_l\mathbf{u}(i) \\ &\hat{\mathbf{y}}_l(i) = \mathbf{C}_l\hat{\mathbf{x}}_l(i), \quad \mathbf{y}_l(i) = \rho_l\tilde{\mathbf{y}}_l(i), \quad \hat{\mathbf{x}}_l(0) = \hat{\mathbf{x}}_{l0} \end{aligned}. \tag{45}$$

Exploiting coordinate decomposition, the gain matrix $\mathbf{L}_l$ includes only nine non-zero gains dependent on the predictor eigenvalue set Λ_l. The same is valid also for the angular acceleration predictor.

7.2 Attitude state predictor

The attitude predictor is a constrained-gain one [11], exploiting coordinate decomposition and error-free attitude kinematics. The key manoeuvre for improving measurement noise filtering is the same as that illustrated in Section 6.2 for the LORF generator: to constrain the correction vector, expressed as $\mathbf{G}_q\mathbf{L}_q\left(\mathbf{y}_q(i)-\mathbf{C}_q\hat{\mathbf{x}}_q(i)\right)$, to belong to the range of $\mathbf{G}_q$, which is lower than the state space size. This implies the predictor can only be stabilized by a dynamic feedback, i.e. a further loop must be added, including the dynamics of the state vector $\mathbf{e}_q$, forced by the output error. Neglecting the star-tracker delay, the state predictor is as follows

$$\begin{aligned}&\begin{vmatrix}\hat{\mathbf{x}}_q\\ \mathbf{e}_q\end{vmatrix}(i+1)=\begin{vmatrix}\mathbf{A}_q & 0\\ 0 & \mathbf{E}_q\end{vmatrix}\begin{vmatrix}\hat{\mathbf{x}}_q\\ \mathbf{e}_q\end{vmatrix}(i)+\begin{vmatrix}\mathbf{B}_q(\mathbf{q})\\ 0\end{vmatrix}\begin{vmatrix}\hat{\mathbf{a}}_a\\ \hat{\omega}_O\end{vmatrix}(i)+\left|\begin{array}{c|c}\mathbf{G}_q\mathbf{L}_q & \mathbf{G}_q\mathbf{L}_e\\ I & 0\end{array}\right|\begin{vmatrix}\mathbf{y}_q(i)-\mathbf{C}_q\hat{\mathbf{x}}_q(i)\\ \mathbf{e}_q\end{vmatrix}.\\ &\hat{\mathbf{y}}_q(i)=\mathbf{C}_q\hat{\mathbf{x}}_q(i)\end{aligned} \tag{46}$$

The eigenvalue set is denoted by Λ_q. The attitude measure $\mathbf{y}_q(i)$ is obtained from the attitude matrix (see Section 4.3.3)

$$\mathbf{Y}_q(i)=\hat{\mathbf{R}}_O(i)\mathbf{R}_s(i)\mathbf{R}_{s0}^T. \tag{47}$$

7.3 Eigenvalue tuning

Internal stability. The closed-loop system composed of the design model, free of modeling errors, and of the attitude and drag-free control laws (driven by the relevant state predictors), can be shown to be internally stable, if and only if the eigenvalue sets $\Lambda_l, \Lambda_a, \Lambda_q, \Lambda_g$ and Λ_{cq} are within the unit disk. In this case, the unstable dynamics of the unknown disturbance classes become completely disconnected from the controllable dynamics, being replaced by the bounded and command-independent error $\hat{\mathbf{e}}(i)=\mathbf{x}(i)-\hat{\mathbf{x}}(i)$ between the design model state vector $\mathbf{x}$ and the predictor state $\hat{\mathbf{x}}$.

When the measurement vector $\mathbf{y}(i)$ is obtained from the real spacecraft, the assumptions guaranteeing internal stability cease to be valid because of the modeling error $\partial\mathbf{P}_l$ in (30) and structured uncertainties mentioned in Section 5.4.2. Their effects spill through plant measures $\mathbf{y}$ making the estimation error $\hat{\mathbf{e}}$ to be command-dependent via an uncertain dynamic operator $\hat{\mathbf{e}}=\mathbf{E}_x\left(\mathbf{y}_0(\mathbf{u},\mathbf{w})\right)$. By restricting our considerations to linear drag-free control, output error $\hat{\mathbf{e}}_{yl}=\mathbf{y}_{0l}-\hat{\mathbf{y}}_l$, and model error $\partial\mathbf{P}_l$, the operator can be expressed as

$$\hat{\mathbf{e}}_{yl}=\mathbf{E}_{yl}\left(\mathbf{y}_{0l}(\mathbf{u},\mathbf{w})\right)=\mathbf{V}_{ol}\left(\partial\mathbf{P}_l\left(\mathbf{y}_{0l}(\mathbf{u},\mathbf{w})\right)\right) \tag{48}$$

where $\mathbf{V}_{ol}$ is the dynamic operator of the acceleration state-predictor, in Section 7.1, mapping the measure $\mathbf{y}_{ol}$ to the estimate $\hat{\mathbf{y}}_l$. According to [10], one way to recover closed-loop stability in the presence of uncertain modeling errors,, is to assign the predictor eigenvalue set Λ_l to the unit disk so as to sufficiently bound the effect of $\mathbf{E}_{yl}$ on the estimation error $\hat{\mathbf{e}}_{yl}$. Formally, if the predictor operator $\mathbf{V}_{ol}$ is designed such as to guarantee that $\mathbf{E}_{yl}$ satisfies the norm inequality

$$\left\|\hat{\mathbf{e}}_{yl}\right\| < \eta_y \left\|\mathbf{y}_0\right\| + \eta_0, \quad \eta_y < 1, \quad \eta_0 < \infty \quad , \tag{49}$$

the DFAC, designed by neglecting modeling errors, stabilizes the real closed-loop system. In practice, the state-predictor design forces the ensemble 'plant+state-predictor', mapping $\mathbf{u}$ to $\hat{\mathbf{y}}_l$, to approach the design model so as to keep stability and performances as predicted by the model-based control laws (43) and (44). The scalar η_y is the norm of the operator $\mathbf{E}_{yl}$ and η_0 is a bound to $\mathbf{w}$ effects. The inequality of Eq. (49), although sufficient to recover stability, is not sufficient to recover model-based performance. The latter can be recovered by lowering η_y and η_0. Because only approximate versions of inequality (49) can be obtained analytically, the simulated fine model provides a test-bed of the critical and uncertain dynamics, whereby to guarantee *a priori* stability and performance. Analytic computation of η_y and η_0, made by a simple model of $\partial\mathbf{P}_l$, like Eq. (33), may provide initial values of the control parameters to be refined by simulated runs. For instance, by employing H_∞ norms as in Eq. (34), fixing the predictor eigenvalue set of a generic coordinate *x* to $\Lambda_{lx} = \{1-\gamma, 1-\gamma, 1-2\gamma\}$ and imposing some margin to Eq. (49), the relation

$$\eta_y = \left\|\mathbf{V}_{ol} \cdot \partial\mathbf{P}_l\right\|_\infty \cong \left|\gamma\left(1-2.5\gamma\right)\right| 2 \le 1/5 < 1 \tag{50}$$

suggests the eigenvalue set $\Lambda_{lx} = \{0.4, 0.8, 0.8\}$. These values appear compatible with the requested closed-loop bandwidth (Control Issue 3). The range assigned to the eigenvalue sets is shown in Table 8.

Table 8 Eigenvalue sets of the DFAC.

Set	Λ_l, Λ_a	Λ_q	Λ_g	Λ_{cq}
Range	0.3÷0.8	0.999÷0.9995	0.998÷ 0.99995	0.95÷0.99
Size	18	15	12	6

8 Simulated results

Two main issues concerned the drag-free and attitude control design presented in this paper. The first is the *robustness* of DFAC accuracy performances faced with spacecraft and environment uncertainties, like mass and inertia variations, thrust misalignments, and thermosphere density variation due to delayed launch (Control Issue 2). Figure 12 and Figure 13show the spectral densities of the residual linear accelerations and of the different attitude variables (angular accelerations, rates and attitude angles), under worst-case spacecraft and environment conditions. They are compared to the target bound profiles defined in Table 3.

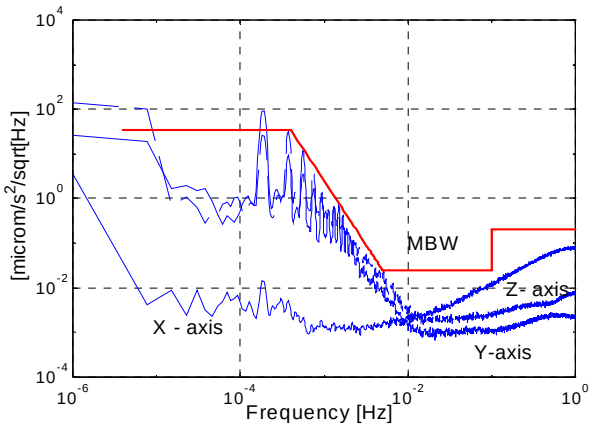

Figure 12. SD of the residual linear accelerations compared to target bound. Ordinate: $\mu m/s^2 / \sqrt{Hz}$

Target accuracy is met with a good margin in the most significant region for gradiometer measurements, i.e. from MBW up to $f_c / 2$. Accuracy appears somewhat critical at low frequencies with regard to cross-axis residual accelerations a_{ly}, a_{lz}. But this is the price to pay for the thrust-peak minimizing strategy (LF strategy) in Section 6.3. The DC component of the attitude PSD is due to worst-case star-tracker bias.

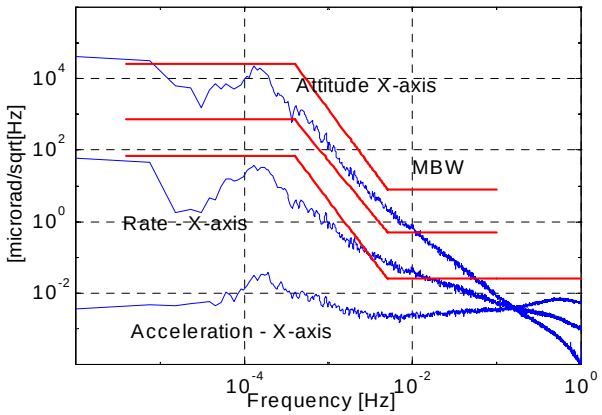

Figure 13. PSDs of the satellite roll $\left[\mu\text{rad}/\sqrt{\text{Hz}}\right]$, of the relevant angular rate $\left[\mu\text{rad/s}/\sqrt{\text{Hz}}\right]$ and residual angular acceleration $\left[\mu\text{rad/s}^2/\sqrt{\text{Hz}}\right]$.

The second issue is the compatibility and sizing of electric micro-propulsion to guarantee the required thrust authority with some margin. Table 9 shows the progressive reduction of the average and peak thrust of the micro-thruster assembly (Control Issue 4), which may be obtained by applying the LP and LF command distribution strategies. LF strategy is very effective in peak and average thrust reduction. LP allows a saving of about 25% of propellant/energy.

Table 9 Comparison of command distribution strategies.

Strategy		Ion-thruster [mN]		Micro-thruster [mN]	
LF	LP	Average	Peak	Average	Peak
No	No	9.78	20.55	2.49	1.06
No	Yes			1.88	0.99
Yes	No			1.26	0.55
Yes	Yes			0.93	0.51

9 Conclusions

In this paper, the DFAC (Drag-Free and Attitude Control) architecture of the European GOCE (Gravity field and steady-state Ocean Circulation Explorer) satellite was presented: no transition among the several mission phases is considered, and only the science phase is treated in detail. GOCE aims to determine with high accuracy and spatial resolution the Earth's gravity field, through gravity gradiometry and precise orbit determination: the use of these complementary space techniques was explained and discussed in order to establish the requirements for control purpose.

The DFAC is intended to enable operation of the gradiometer for the mission's scientific goals during the six-month operational phases. The Earth's gravity field must be determined in the measurement bandwidth (5mHz to 100mHz), where non-gravitational forces must be counteracted down to micronewton, and spacecraft attitude must track the LORF (Local Orbital Reference Frame) with micro-radian accuracy. In the early GOCE design phase, the DFAC was designed using ion and micro-thrusters as actuators. Then electrical micro-propulsion was abandoned as not being mature, renouncing lateral drag-free control and recovering attitude through magnetic control.

Although still critical from a technology standpoint – to the authors' knowledge electrical micro-thrusters have never flown-, all-propulsion DFAC looks to be the only solution for many future scientific and observation missions,

including next generation gravity missions based on satellite formations. Accordingly, the proposed design and simulated results, to be complemented with formation control as required, are believed to be of interest to the space community.

A further reason of interest may be the control design methodology, built around a discrete-time model of the whole spacecraft and environment dynamics, to be embedded in the control unit itself. Control architecture follows directly and is implemented around the Embedded Model. The resulting architecture is rather similar to Linear Quadratic Gaussian control, but noise statistics does not enter explicitly into the control algorithms, which are thus simpler and more generic; it may however be employed for eigenvalue tuning. Optimization is only sought when command authority has appropriate degrees-of-freedom, as in the case of micro-thruster assembly. Tuning is done by fixing the control-law and state-predictor eigenvalues so as to respect requirements and robustness against model uncertainties.

10 Appendix

10.1 Neglected dynamics

Assume the thruster dynamics to be 2nd order plus a delay as follows

$$\mathbf{P}_t = \frac{e^{-s\tau_t}}{\left(s/\omega_t\right)^2 + 2\zeta_t s/\omega_t + 1},\ \tau_t = 0.01s,\ \omega_t\left(2\pi\right)^{-1} = 10\text{ Hz},\quad \zeta_t = 0.7\,. \tag{51}$$

Then assume a 4th order anti-aliasing filter designed to avoid any folding of the f^2 noise of the gradiometer measurements, as follows

$$\mathbf{P}_a = \frac{e^{-s\tau_a}}{\left(s/\omega_a\right)^4 + \alpha_1\left(s/\omega_a\right)^3 + \alpha_2\left(s/\omega_a\right)^2 + \alpha_1 s/\omega_a + 1}\,. \tag{52}$$
$$\tau_a = 0.01s;\quad \omega_a\left(2\pi\right)^{-1} = 5\text{ Hz}$$

The overall thruster-to-gradiometer dynamics $\mathbf{P}_l$ can be written as follows, upon introducing a fractional gain error ∂b :

$$\mathbf{P}_l = \left(1+\partial b\right)\mathbf{P}_t\mathbf{P}_a,\quad \left|\partial b\right| < 0.09\,. \tag{53}$$

Assuming a pure delay in the design model, i.e.

$$\mathbf{M}_l = e^{-sT},\quad T = 0.1s\,, \tag{54}$$

the fractional error dynamics $\partial\mathbf{P}$ can be written as

$$\partial\mathbf{P}_l = \left(1+\partial b\right)\mathbf{P}_t\mathbf{P}_a\mathbf{M}_l^{-1} - 1\,. \tag{55}$$

Converting Eq. (55) into Z-transform, under assumption of zero-order-hold interpolation, and making some approximations, yields the expression in Eq. (33). The harmonic response in Eq. (33) – open-loop error dynamics - and the same filtered by the state-predictor transfer-function $\mathbf{V}_{ol}$ as in Eq. (50) – closed-loop error dynamics - are shown in Figure 14. The closed-loop amplitude $\left|\mathbf{V}_{ol}\cdot\partial\mathbf{P}_I\left(e^{j2\pi fT}\right)\right|$ is always less than 0.2, which guarantees robust closed-loop stability versus uncertainties of $\partial\mathbf{P}$.

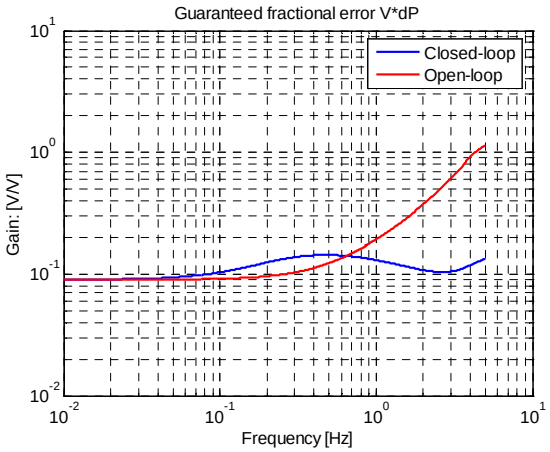

Figure 14. Open-loop and closed-loop fractional error dynamics.

References

[1] Vaníček P. and Krakiwsky E. *Geodesy. The Concepts.* Elsevier, Amsterdam, The Netherlands, 1986.

[2] Tapley B.D., Bettadpur S., Ries J.C., Thompson P.F. and Watkins, M., "GRACE Measurements of Mass Variability in the Earth System", *Science*, Vol. 305, No. 5683, 2004, pp. 503-505.

[3] Koenig R., Zhu S.Y., Reigber Ch., Neumayer K.-H., Meixner H., Galas R., Baustert G. and Schwintzer, P., "CHAMP Rapid Orbit Determination for GPS Atmospheric Limb Sounding", *Advances in Space Research*, Vol. 30, No. 2, 2002, pp. 289-293.

[4] Johannessen J.A and Aguirre-Martinez M. "Gravity Field and Steady-State Ocean Circulation Mission", in *The Four Candidate Earth Explorer Core Missions*. ESA SP-1233, European Space Agency, Noordwijk, The Netherlands, 1999.

[5] DeBra D. B. "Drag-free spacecraft as platforms for space missions and fundamental physics", *Class. Quantum Grav*. Vol. 14, (1997), pp. 1549-1555.

[6] Vaillon L., Duhamel T. and Champetier C. "Advanced AOCS concepts for drag-free applications", in *Proc. 2nd ESA Int. Conf. on GNC, ESA WPP-07*, Noordwijk (The Netherlands), 12-15 April 1994, pp. 353-363.

[7] Canuto E. and Andreis D. "Robust digital control of drag-free satellites", in *Robust Control Design 2003*, Colaneri P., Bittanti S. eds., Elsevier (Oxford, UK, 2004), pp.353-358.

[8] Canuto E., Martella P. and Sechi G. "Attitude and drag control: an application to the GOCE satellite", *Space Science Reviews*, Vol. 108, No. 1, 2003, pp. 357-366.

[9] Leach R. and Neal K.L. "Discussion of micro-newton thruster requirements for a drag-free control system", in *Proc. 16th Annual AIAA/USU Conf. on Small Satellites,* Logan (Utah), 2002, Session VIII, No. 1.

[10] Donati, F. and Vallauri, M. "Guaranteed control of 'almost-linear' plants", *IEEE Trans. on Autom. Control,* Vol. 29, No. 1 1984, pp. 34-41.

[11] Canuto E. "Embedded Model Control: outline of the theory", *ISA Trans.* Vol. 46, No. 3, 2007, pp. 363-377.

[12] Ziegler B. and Blanke M. "Drag-free motion control of satellite for high-precision gravity field mapping", in: *Proc. of 2002 IEEE Int. Conf. on Control Appl.,* 2002, pp. 292-297.

[13] Haines R. "Development of a drag-free control system", in: *Proc. 14th Annual AIAA/USU Conf. on Small satellites,* Logan (Utah), 2000, Session VII, No. 2.

[14] Canuto E. "Drag-Free Control of the GOCE satellite: noise and observer design", submitted to *IEEE Trans. Control Systems Technology*, 2008.

[15] Lange B. "The drag-free satellite", *AIAA Journal,* Vol. 2, No. 9, 1964, pp. 1590-1606.

[16] Vallado D. A., *Fundamentals of Astrodynamics and Applications*, Space Technology Library - Microcosm Press, El Segundo, CA, 2004, pp. 511-524.

[17] Canuto E., Massotti L. "Local orbital frame predictor for LEO drag-free satellites" in *Preprints of the 17th IFAC World Congress*, Seoul (Korea), July 6-11, 2008, pp. 3428-3433.

[18] Fichter W., Gath P., Vitale S. and Bartoluzzi D. "LISA Pathfinder drag-free control and system implications", *Classical and Quantum Gravity* Vol. 22, 2005, pp. S139-S148.

[19] Sechi G., Andrè G., Andreis D. and Saponara M. "Magnetic attitude control of the GOCE satellite", In: *Proc. 6th Int. ESA Conf. on Spacecraft Guidance, Navigation and Control Systems*. Noordwijk (The Netherlands): ESA SP 606, 2006.

[20] Vaillon L., Borde J., Duhamel T, and Damilano P. "Drag-free control systems and technologies", *Space Technol.,* Vol. 16 No. 5/6, 1996, pp. 245-254.

[21] Fichter W., Schleicher A., Szerdahelyi L., Theil S. and Airey P. "Drag-free control system for frame dragging measurements based on cold atom interfrometry", *Acta Astronautica,* Vol. 57, 2005, pp. 788-799.

[22] Canuto E. "Drag-free and attitude control for the GOCE satellite", *Automatica,* Vol. 44, No. July 2008, pp 1766-1780,.

[23] Touboul P., Rodrigues M., Willemenot E. and Bernard A. "Electrostatic accelerometers for the equivalence principle test in space". *Class. Quantum Grav.*, Vol. 13, 1996, pp. A67-A78.

[24] Picone J. M., Hedin A. E., Drob D. P. and Aikin A. C. "NRLMSISE-00 empirical model of the atmosphere: Statistical comparisons and scientific issues", *J. Geophys. Res*. Vol. 107, No. A12, 2002, pp. 1468.